Journal of the Meteorological Society of Japan

EARLY ONLINE RELEASE

The DOI for this manuscript is
DOI:10.2151/jmsj.2019-049
J-STAGE Advance published date: May 17th, 2019

Broadening of cloud droplet size distributions by condensation in turbulence

Izumi Saito, Toshiyuki Gotoh and Takeshi Watanabe

Department of Physical Science and Engineering, Graduate School of Engineering, Nagoya Institute of Technology, Nagoya, Japan

May 3, 2019

Corresponding author: Izumi Saito, Department of Physical Science and Engineering, Graduate School of Engineering, Nagoya Institute of Technology, Gokiso-cho, Showa-ku, Nagoya 466-8555, Japan.
E-mail: izumi@gfd-dennou.org

Abstract

To consider the growth of cloud droplets by condensation in turbulence, the Fokker-Planck equation is derived for the droplet size distribution (droplet spectrum). This is an extension of the statistical theory proposed by Chandrakar and coauthors in 2016 for explaining the broadening of the droplet spectrum obtained from the 'Π-chamber', a laboratory cloud chamber. In this Fokker-Planck equation, the diffusion term represents the broadening effect of the supersaturation fluctuation on the droplet spectrum. The aerosol (curvature and solute) effects are introduced into the Fokker-Planck equation as the zero flux boundary condition at $R^2 = 0$, where R is the droplet radius, which is mathematically equivalent to the case of Brownian motion in the presence of a wall. The analytical expression for the droplet spectrum in the steady state is obtained and shown to be proportional to $R\exp(-cR^2)$, where c is a constant. We conduct direct numerical simulations of cloud droplets in turbulence and show that the results agree closely with the theoretical predictions and, when the computational domain is large enough to be comparable to the Π-chamber, agree with the results from the Π-chamber as well. We also show that the diffusion coefficient in the Fokker-Planck equation should be expressed in terms of the Lagrangian autocorrelation time of the supersaturation fluctuation in turbulent flow.

Keywords cloud droplet size distribution, turbulence-cloud droplet interaction, Fokker-Planck equation, direct numerical simulation

1. Introduction

Clouds play a crucial role in Earth's weather and climate system, yet our understanding of clouds remains limited. One of the challenges in improving understanding is the vast range of scales involved. If we focus on clouds without ice (so-called 'warm clouds', Lau and Wu 2003), the relevant processes range from the condensation-nucleation of aerosol particles at nanometer scales, to the condensation growth of droplets at scales of a few to several tens of micrometers, then to the collision-coalescence growth of hundreds of micrometers up to raindrops on scales of millimeters (Houze 2014). Furthermore, because flows inside clouds are inherently turbulent, they involve various sizes of eddies and associated fluctuations, ranging from the largest energy-containing scale of a few kilometers to the smallest scale of a few millimeters where the molecular viscosity is dominant. These turbulent eddies interact with each other, and interact with the droplets as well, making the modeling and understanding of cloud turbulence a highly complex problem (Bodenschatz et al. 2010).

The turbulence properties of clouds have been revealed by recent high-resolution in-situ measurements (Siebert et al. 2006, 2015; Bodenschatz

2015; Risius et al. 2015). For example, Siebert and Shaw (2017) used helicopter-borne measurements and observed the fine-scale turbulence structures of cumulus clouds newly formed in the atmospheric boundary layer. From temperature and humidity measurements with resolutions as high as several tens of centimeters, they demonstrated that the supersaturation fluctuation has an amplitude on the order 1%.

Because of its potential importance for the growth of droplets in clouds, turbulence has been investigated as one of the key candidates for improving numerical weather models and cloud microphysical parameterizations (Vaillancourt and Yau 2000; Shaw 2003; Devenish et al. 2012; Grabowski and Wang 2013). Although clarifying the effect of turbulence in clouds is not an easy task as the turbulence itself is still not fully understood (Frisch 1995; Wyngaard 2010; Davidson et al. 2012), recent developments in high-performance supercomputers have made it possible to conduct direct numerical simulations (DNSs) of cloud turbulence, and numerous studies have been carried out since the pioneering work by Vaillancourt et al. (2001, 2002).

For condensation growth, turbulent mixing and entrainment in clouds excite strong spatial and temporal fluctuations in temperature and humidity. These turbulent fluctuations cause differences in the local supersaturation experienced by each droplet, which in turn cause differences in

the growth histories of droplets and a broader droplet size distribution. This mechanism was examined since the early 1960s by a group of studies known as the "stochastic condensation theory" (mostly Russian, see Sedunov 1974; Clark and Hall 1979; Korolev and Mazin 2003), but the importance of the mechanism was later reinforced by Cooper (1989) and a sophisticated microphysical Lagrangian model by Lasher-Trapp et al. (2005). DNSs on condensation growth of cloud droplets in a turbulent environment have been conducted and revealed various features, such as the essential role of large-scale turbulent motions, the fine-scale structures at the cloudy-clear air interface, and two-way coupling between the supersaturation fluctuation and cloud droplets (Celani et al. 2005, 2009; Lanotte et al. 2009; Sardina et al. 2015; Kumar et al. 2014, 2018).

For collision growth, vertically straight trajectories of gravitationally sedimenting droplets are perturbed by turbulent fluctuations in the air velocity field. Moreover, the acceleration of droplets due to the turbulent velocity field can be comparable to gravitational acceleration, causing complex droplet trajectories and phenomena such as the inertial clustering effect (Sundaram and Collins 1997) and the sling effect (Falkovich and Pumir 2007). This leads to the enhancement of the collision rate especially among droplets of similar sizes and to accelerated rain initiation (Franklin et al. 2005; Ayala et al. 2008b; Onishi et al. 2015; Chen et al. 2018a).

The knowledge accumulated from above studies has resulted in the development and implementation of new cloud microphysical parameterizations that account for the effect of turbulence on the condensation growth (Grabowski and Abade 2017; Sardina et al. 2018) or on the collision-coalescence growth of droplets (Franklin et al. 2007; Grabowski and Wang 2009; Ayala et al. 2008a; Seifert et al. 2010; Onishi and Seifert 2016). In addition, several studies have conducted DNSs including both the condensation and collision-coalescence processes in order to obtain a more comprehensive understanding of the effect of turbulence on the continuous growth of droplets (Chen et al. 2018b; Saito and Gotoh 2018; Kunishima and Onishi 2018).

On the other hand, an interesting laboratory experiment was recently conducted by Chandrakar et al. (2016) (hereinafter referred to as "C16") which focused on the effect of turbulence on the condensation growth of cloud droplets. They used a laboratory chamber with a working volume of $3.14\mathrm{m}^3$, referred to as the "Π-chamber" (Chang et al. 2016), and produced a steady state turbulent cloud in the chamber in the following way. Moist Rayleigh-Benard convection is excited in the chamber to produce turbulent fluctuations in the air velocity and supersaturation fields. Aerosol particles are injected into the system at a constant rate, removed from the system by sedimentation, and the steady state particle number density is determined

through the balance between the source and sink. Aerosol particles initiate the generation of cloud droplets in the moist air, and their sizes change in the fluctuating supersaturation field. The droplet size distributions in statistically steady states were measured and demonstrated to be narrower for experiments with greater number densities of cloud droplets. This tendency is associated with the dispersion aerosol indirect effect (Chandrakar et al. 2018b). In C16, a statistical theory was also proposed to account for their experimental results, and it was shown that this theory can explain the statistical properties of the droplet size distribution fairly well for a certain range of experimental parameters.

Although there are differences in the physical parameters and conditions of atmospheric clouds and the laboratory clouds in C16, we believe that the Π-chamber experiment is highly useful for validating the results of numerical simulations for the following reasons. First, in contrast to cloud observation in the atmosphere, the Π-chamber experiment provides detailed information on the laboratory cloud which was obtained under closely controlled laboratory conditions. This is useful for comparing between the laboratory experiment and numerical simulations, and for the identifying important factors for droplet growth in turbulent clouds. Second, the chamber's volume of about $3\mathrm{m}^3$ is achievable in DNSs. For example, resolving the smallest turbulent motion requires a grid length of about 1-2 mm. With this grid

length, we need about 1000^3 grid points to fill a domain of 3m^3, which is feasible with recent high-performance computers. Thus, the inter-comparison of the laboratory experiment, DNSs, and statistical theory is possible, which is useful and important for a deeper understanding of cloud microphysical processes. It also should be noted that the domain size of 3 m^3 is close to the finest grid size used in the latest high-resolution large-eddy simulations (LESs) of clouds (Sato et al. 2018) ($\Delta x = \Delta y = 6.25\text{m}$, $\Delta z = 5\text{m}$). This suggests that useful knowledge on cloud microphysical processes can be provided from DNSs to LESs with little extrapolation.

With the above motivation, the main purpose of the present study is to conduct DNSs using our DNS model the "cloud microphysics simulator" (Gotoh et al. 2016), and compare the results with the statistical theory and the laboratory experiment by C16. First, we make several extensions to the statistical theory by C16. We obtain an analytical expression for the droplet size distribution at a steady state by deriving the Fokker-Planck equation for the droplet size distribution. Aerosol (curvature and solute) effects on droplet growth are introduced as the zero flux boundary condition, which is mathematically equivalent to the case of Brownian motion in the presence of a wall. Next, we compare this theory with the experimental results of a small-scale DNS (box length is $L_{\text{box}} = 12.8\text{cm}$). Finally, we conduct a large-scale DNS ($L_{\text{box}} = 102.4\text{cm}$) with a domain size comparable to the

size of the Π-chamber.

Readers should be aware that our target in this study is the Π-chamber experiment by C16 and the physical parameters and conditions are accordingly different from those in atmospheric clouds. Therefore the interpretation of the present results needs great care in the context of atmospheric clouds. We discuss these points in detail in Sec. 4.

The remainder of the present paper is organized as follows. In Sec. 2, we consider the statistical theory proposed in C16 and its extension. In Sec. 3, we conduct DNSs. A discussion and summary are provided in Sec. 4 and Sec. 5, respectively.

2. Statistical theory by Chandrakar et al. (2016) and its extension

Before introducing our extensions, we first briefly review the statistical theory proposed by C16. First, the size of the cloud droplet evolves in response to the ambient supersaturation as

$$\frac{dR^2}{dt} = 2K_{\rm s}S, \tag{1}$$

where R is the droplet radius, S is the supersaturation at the droplet position, and $K_{\rm s}$ is assumed to be constant for simplicity. Second, the evolution of the supersaturation is assumed to be given by the following stochastic

differential equation:

$$\begin{aligned} dS(t) &= S(t+dt) - S(t) \\ &= \left[\frac{S_{\rm eq} - S}{\tau_{\rm t}} - \frac{S}{\tau_{\rm c}}\right] dt + \left(\frac{2\sigma_{S_0}^2 dt}{\tau_{\rm t}}\right)^{1/2} \xi(t) \end{aligned} \tag{2}$$

where σ_{S_0} is the standard deviation of the supersaturation without cloud droplets, $S_{\rm eq}$ is the equilibrium value of the supersaturation, $\xi(t)$ is a Gaussian white noise process with a zero mean:

$$< \xi(t) >= 0, \tag{3}$$

$\delta()$ is the Dirac delta, and angle brackets indicate the ensemble average.

In (2), the effects of the turbulent fluctuation of the supersaturation are represented in terms of $\tau_{\rm t}$ based on a Langevin model, where $\tau_{\rm t}$ is referred to as the turbulent mixing time [Here we simply refer to $\tau_{\rm t}$ as the turbulent mixing time and determine the appropriate value for $\tau_{\rm t}$ from the simulation results in Sec. 3]. On the other hand, the term with $\tau_{\rm c}$ in (2) represents the effect of cloud droplets on the supersaturation through condensation/evaporation. The parameter $\tau_{\rm c}$ is referred to as the phase relaxation time (Cooper 1989), and is inversely related to the number density $n_{\rm d}$ and mean radius of cloud droplets by

$$\tau_{\rm c}^{-1} \propto n_{\rm d} \overline{R}, \tag{4}$$

where the overbar denotes the volume average. See Appendix A for the precise form of $\tau_{\rm c}$.

Using (1) and (2), C16 derived estimates of the statistical properties of the supersaturation fluctuation and the droplet size distribution for a statistically steady state. Here, the number density n_{d} is assumed to be constant due to the balance between the injection and removal of cloud droplets, and cloud droplets are assumed to remain in the system with a residence time τ_{res}. The variance of the supersaturation is given by

$$\sigma_S^2 = \overline{(S')^2} = \frac{\tau_{\mathrm{s}}}{\tau_{\mathrm{t}}}\sigma_{S_0}^2 \ \left(< \sigma_{S_0}^2\right), \tag{5}$$

where $S' = S - \overline{S}$ is the supersaturation fluctuation. The variance of the squared radius is given by

$$\sigma_{R^2}^2 = \frac{8K_{\mathrm{s}}^2\sigma_{S_0}^2\tau_{\mathrm{s}}^2}{\tau_{\mathrm{t}}}\tau_{\mathrm{res}}, \tag{6}$$

where τ_{s} is referred to as the system timescale and is given by the harmonic mean of τ_{t} and τ_{c} as

$$\tau_{\mathrm{s}} = \left(\frac{1}{\tau_{\mathrm{t}}} + \frac{1}{\tau_{\mathrm{c}}}\right)^{-1} = \frac{\tau_{\mathrm{t}}\tau_{\mathrm{c}}}{\tau_{\mathrm{t}} + \tau_{\mathrm{c}}}. \tag{7}$$

See C16 for the detailed derivations of (5) and (6).

2.1 Physical interpretation and Fokker-Planck equation

The above statistical theory by C16 describes the interaction between cloud droplets and the supersaturation fluctuation in what is assumed to be the most straightforward way. First, the effect of cloud droplets on

the supersaturation fluctuation is described in (5). If the supersaturation is positive/negative, cloud droplets make the ambient air drier/moister by condensation/evaporation, respectively. The overall effect is that they reduce the amplitude of the supersaturation fluctuation and $\sigma_S < \sigma_{S_0}$. Second, the effect of the supersaturation fluctuation on cloud droplets is described in (6). As the amplitude of the supersaturation fluctuation (σ_{S_0}) increases, the droplet size distribution becomes broader and σ_{R^2} increases.

We can also understand the above theory through an analogy with Brownian theory. From (1) and (2), we can regard R^2 and $2K_{\rm s}S$ as the position and velocity of Brownian particles, respectively, and rewrite (6) as

$$\sigma_{R^2}^2 = 2D\tau_{\rm res}, \tag{8}$$

where D is the diffusion coefficient for Brownian motion given by

$$D = \left[4K_{\rm s}^2\sigma_S^2\right]\tau_1 = \left[4K_{\rm s}^2\left(\sigma_{S_0}^2\frac{\tau_{\rm s}}{\tau_{\rm t}}\right)\right]\tau_1. \tag{9}$$

Just like the spatial distribution of Brownian particles, the droplet size distribution diffuses due to the supersaturation fluctuation σ_S. For the time parameter τ_1 in (9), the C16 result (6) is recovered if we substitute the system timescale $\tau_{\rm s}$ for τ_1 as

$$\tau_1 = \tau_{\rm s}. \tag{10}$$

Based on the analogy with Brownian motion, we can extend the above theory to consider the evolution of the size distribution. Since we can regard

the squared radius of cloud droplets (R^2) as the position of the Brownian particles with the diffusion coefficient D given by (9), the size distribution for R^2, or $n(R^2, t)$, evolves according to the following Fokker-Planck equation:

$$\frac{\partial n(R^2,t)}{\partial t} = D\frac{\partial^2 n(R^2,t)}{\partial (R^2)^2} - \frac{1}{\tau_{\rm res}} n(R^2,t) + J_0 \delta(R^2 - R_0^2). \tag{11}$$

The first term on the right side in (11) represents the broadening effect of the supersaturation fluctuation. For simplicity, the diffusion coefficient D is assumed to be constant. The term with $\tau_{\rm res}$ represents the sink, where cloud droplets are removed from the system with a residence time of $\tau_{\rm res}$. The term with J_0 represents the source, where cloud droplets are injected into the system at a constant rate J_0 and an injection radius R_0.

The boundary condition is essential to determine the distribution function. When the radius of a cloud droplet is small, the evolution equation (1) is no longer valid. We should consider the curvature and solute effects, which we hereinafter simply refer to as "aerosol effects", and terms associated with the Köhler curve are introduced as explained later in (31). This is the case for the Π-chamber, since aerosol particles are injected into the chamber with initial radii ranging from several tens to hundreds of nanometers.

As a simple way to include the aerosol effects in the theoretical framework, we adopt the idea by Siewert et al. (2017). To a first approximation,

the effect of the Köhler curve is to keep the droplet radius positive. More precisely, even when the supersaturation in the ambient air is negative, the droplet radius is kept at the corresponding equilibrium radius, which is small but positive definite. Siewert et al. (2017) suggested that this effect can be approximated with a reflecting wall boundary condition as in the case of Brownian motion, which is mathematically equivalent to the zero flux boundary condition at $R^2 = 0$ as

$$\frac{\partial n(R^2, t)}{\partial R^2} = 0, \quad \text{at} \;\; R^2 = 0. \tag{12}$$

For $R^2 \to \infty$ it is natural to assume that

$$n(R^2, t) \to 0 \quad \text{for} \quad R^2 \to \infty, \tag{13}$$

and the initial condition is

$$n(R^2, 0) = n_0(R^2). \tag{14}$$

The analytical solution for the above model is given in Appendix E (Chandrasekhar 1943), but hereafter we examine only the steady state solution for two typical cases, case a) : R_0 is large such that $R_0^2 \gg R_*^2$, and case b) : R_0 is small such that $R_0^2 \sim R_*^2$, where R_* is a characteristic radius at which the Köhler curve attains the maximum and the aerosol effects become appreciable.

a. Steady state size distribution when the injection radius is large

For the steady state ($\partial/\partial t = 0$) where all three fluxes (source, sink, and flux due to the diffusion of particles in R^2-space) balance each other, we can obtain an analytical solution of (11). In the present case, the probability density function (PDF) of R^2 for the solution is given as follows:

$$\mathrm{P}(R^2) = \frac{1}{2\beta^2} \exp\left(-\beta^{-2}|R^2 - R_0^2|\right), \tag{15}$$

where β has the dimension of length and is defined as

$$\beta = (D\tau_{\mathrm{res}})^{1/4}. \tag{16}$$

From (15), the average of R^2 and the variance are given by

$$\overline{R^2} = \int_0^\infty R^2 \mathrm{P}(R^2) dR^2 = R_0^2, \tag{17}$$

$$\sigma_{R^2}^2 = \int_0^\infty (R^2 - \overline{R^2})^2 \mathrm{P}(R^2) dR^2 = 2\beta^4 = 2D\tau_{\mathrm{res}}, \tag{18}$$

respectively, where we additionally assumed that $R_0 \gg \beta$. Equation (18) agrees with (8).

b. Steady state size distribution when the injection radius is small

The solution of the Fokker-Planck equation in this case is found to be

$$\begin{aligned} \mathrm{P}(R^2) &= \frac{1}{2\beta^2} \exp\left(-\beta^{-2}|R^2 - R_0^2|\right) \\ &\quad + \frac{1}{2\beta^2} \exp\left(-\beta^{-2}|R^2 + R_0^2|\right), \qquad (R^2 > 0). \end{aligned} \tag{19}$$

Taking the limit $R_0 \to 0$ for simplicity, the PDF of R^2 in the steady state is given by

$$\mathrm{P}(R^2) = \frac{1}{\beta^2} \exp\left(-\beta^{-2} R^2\right). \tag{20}$$

The average of R^2 is given by

$$\overline{R^2} = \int_0^\infty R^2 \mathrm{P}(R^2) dR^2 = \beta^2, \tag{21}$$

which is different from $R_0^2 (\approx 0)$ for the source. This difference is due to the presence of the reflecting wall and differs from the result obtained without aerosol effects (17). The variance of R^2 is given by

$$\begin{aligned} \sigma_{R^2}^2 &= \int_0^\infty (R^2 - \overline{R^2})^2 \mathrm{P}(R^2) dR^2 \\ &= \beta^4 = D\tau_{\mathrm{res}}, \end{aligned} \tag{22}$$

which does not have the factor 2, in contrast to (18). The statistical properties of the distribution (20) are summarized in Appendix D.

Several studies on cloud turbulence used the Fokker-Planck equation to derive the droplet size distribution for the steady state, but with slightly different settings (McGraw and Liu 2006; Siewert et al. 2017). For example, McGraw and Liu (2006) obtained the same functional form as (20), but their Fokker-Planck equation did not include the source and sink terms and required a negative mean supersaturation to attain a steady state size distribution. We consider the effect of the mean supersaturation later in (53).

3. Numerical experiments

Here, we conduct DNSs of cloud droplets in turbulence and compare the results with the theory in the previous section. The numerical domain under consideration is a cubic box with sides of length $L_{\rm box}$ which is assumed to be in the chamber interior far from the wall. We also assume that $L_{\rm box}$ is sufficiently small. Accordingly, the turbulence is regarded as being homogeneous isotropic and periodic boundary conditions in three directions are applied.

3.1 Governing equations

a. Fluid

The velocity field of air is governed by the incompressible Navier-Stokes equations:

$$\begin{aligned} \frac{\partial \mathbf{u}}{\partial t} + \mathbf{u}\cdot\nabla\mathbf{u} &= -\frac{1}{\rho_{\rm a}}\nabla p + \nu_{\rm a}\nabla^2\mathbf{u} + \mathbf{f}, \\ \nabla\cdot\mathbf{u} &= 0, \end{aligned} \tag{23}$$

where p is the pressure fluctuation, $\rho_{\rm a}$ and $\nu_{\rm a}$ are the density and kinematic viscosity of dry air, respectively, and $\mathbf{f}$ represents the external force for the velocity field. The temperature T and the water vapor mixing ratio Q are expressed as the sum of the mean and fluctuation as

$$T = \overline{T} + \theta, \tag{24}$$

$$Q = \overline{Q} + q, \tag{25}$$

297 respectively, where the overbar denotes the volume average over the box.
298 The evolution equations for θ and q are given by

$$\frac{\partial \theta}{\partial t} + \mathbf{u} \cdot \nabla \theta = \frac{L_{\mathrm{v}}}{c_{\mathrm{p}}} \left(C_{\mathrm{d}} - \overline{C}_{\mathrm{d}} \right) + \kappa_{\mathrm{T}} \nabla^2 \theta + f_\theta, \tag{26}$$

$$\frac{\partial q}{\partial t} + \mathbf{u} \cdot \nabla q = - \left(C_{\mathrm{d}} - \overline{C}_{\mathrm{d}} \right) + \kappa_{\mathrm{v}} \nabla^2 q + f_q, \tag{27}$$

299 where κ_{T} and κ_{v} are the thermal diffusivity and diffusivity of water vapor,
300 respectively, L_{v} is the latent heat of vaporization, c_{p} is the specific heat of
301 air at constant pressure, and C_{d} is the condensation rate defined later in
302 (34). f_θ and f_q represent the external forces on θ and q, respectively.

303 We next consider evolution equations for the mean values, $\overline{T}$ and $\overline{Q}$.
304 In the Π-chamber, the moist Rayleigh-Benard convection and turbulence
305 keep the chamber interior in a statistically steady state, and $\overline{T}$ and $\overline{Q}$ are
306 accordingly kept at statistically steady values. As a simple model for this
307 effect, we use nudging terms as follows:

$$\frac{\partial \overline{T}}{\partial t} = \frac{L_{\mathrm{v}}}{c_{\mathrm{p}}} \overline{C}_{\mathrm{d}} - \frac{\overline{T} - T_0}{\tau_0}, \tag{28}$$

$$\frac{\partial \overline{Q}}{\partial t} = - \overline{C}_{\mathrm{d}} - \frac{\overline{Q} - Q_0}{\tau_0}, \tag{29}$$

308 where terms with τ_0 mean that the average values are nudged to T_0 and Q_0
309 with a timescale τ_0.

b. Particles

Cloud droplets are assumed to be smaller than the grid size and are treated as point particles. The evolution equations for the jth cloud droplet are given by

$$\frac{d\mathbf{X}_j(t)}{dt} = \mathbf{u}\left(\mathbf{X}_j\right), \tag{30}$$

$$\frac{dR_j(t)^2}{dt} = 2K_{\rm s}\left[S(\mathbf{X}_j) - \frac{A}{R_j(t)} + \frac{B}{R_j(t)^3}\right], \tag{31}$$

where $\mathbf{X}_j(t)$ and $R_j(t)$ are the position and radius, respectively, of the j-th cloud droplet, and $\mathbf{u}\left(\mathbf{X}_j\right)$ and $S(\mathbf{X}_j)$ are the fluid velocity and supersaturation, respectively, at the droplet position. The parameter $K_{\rm s}$ is a diffusion coefficient for droplet growth that depends on the pressure and temperature (Pruppacher and Klett 1997). $K_{\rm s}$ is set to a constant because its fluctuations are sufficiently small in the present DNS. Terms with A and B in (31) represent the curvature and solute effects, respectively, definitions of which are given in Appendix B.

The supersaturation at the droplet position, $S(\mathbf{X}_j(t), t)$ in (31), is defined by

$$S\left(\mathbf{X}_j(t), t\right) = \frac{Q\left(\mathbf{X}_j(t), t\right)}{Q_{\rm vs}\left(\mathbf{X}_j(t), t\right)} - 1. \tag{32}$$

The saturation mixing ratio for the water vapor $Q_{\rm vs}$ at the droplet position is determined by Tetens' formula:

$$Q_{\rm vs}(\mathbf{X}_j(t), t) = \varepsilon_0 \frac{610.78}{P_0} \exp\left[17.629 \frac{T(\mathbf{X}_j(t), t) - 273.16}{T(\mathbf{X}_j(t), t) - 35.86}\right], \tag{33}$$

where $\varepsilon_0 = R_\mathrm{d}/R_\mathrm{v} \approx 0.62$, R_d and R_v are the gas constants for dry air and water vapor, respectively, and P_0 is the environmental pressure.

Note that there are several properties of the droplet dynamics that are neglected in the present DNS, such as gravity, droplet inertia, and collision-coalescence. The reason for these simplifications is to make the model in our DNS simpler and closer to that in the statistical theory in Sec. 2 to facilitate a comparison between the two. Possible effects of these simplifications are discussed in Sec. 5.

The droplet size changes according to (31). The condensation rate $C_\mathrm{d}(\mathbf{x}, t)$ in (26) and (27) is then calculated by

$$C_\mathrm{d}(\mathbf{x}, t) = \frac{1}{\rho_\mathrm{a}(\Delta x)^3} \sum_{j=1}^{N_\Delta} \frac{dm_j(t)}{dt}, \tag{34}$$

where N_Δ is the number of cloud droplets within the grid cell $(\Delta x)^3$ and m_j is the mass of the j-th cloud droplet defined as

$$m_j(t) = \frac{4\pi}{3} \rho_\mathrm{w} R_j(t)^3, \tag{35}$$

where ρ_w is the liquid water density.

3.2 Experimental setup

a. Nudging and thermodynamic parameters

We assumed that the environmental pressure P_0 was 1013.25 hPa (= 1 atm) and that the mean temperature in the domain was kept close to

290 K. Accordingly, we set the nudging parameter as $T_0 = 290$ K in (28). Other parameters are summarized in Table 1. With these parameters, the diffusion coefficient K_s in (31) was estimated as $K_s = 1.097 \times 10^{-6}$ cm^{2}s^{-1} for sufficiently dilute drop (Pruppacher and Klett 1997). Table 1

For parameter Q_0 in (29), we set Q_0 so that the corresponding supersaturation $S_0(T_0, Q_0)$ was 0 % based on (32) and (33). The value of Q_0 used in the present DNS is shown in Table 1. The reason for this choice of S_0 is that the main focus of the present study is on the effect of the supersaturation fluctuation. We discuss the effect of this choice of S_0 in Sec. 3.4.

For the nudging timescale τ_0, we assume that $\overline{T}$ and $\overline{Q}$ are mainly determined by the largest eddies. We set $\tau_0 = 0.9$ s and $\tau_0 = 2.0$ s for the small- and large-scale DNS, respectively. These values are roughly consistent with the large-eddy turnover time (see Table 2). Table 2

b. Solute Fig. 1

The solute dissolved in each cloud droplet is NaCl (sodium chloride). For simplicity, the amount of solute is fixed to $m_s = 1.13 \times 10^{-15}$g, which corresponds to a sphere with an equivalent radius of 50 nm. The parameters for the aerosol effects are summarized in Appendix B. With these parameters, from the definitions in (59) and (60) we have $A = 1.089 \times 10^{-7}$ cm and $B = 1.665 \times 10^{-16}$ cm^3, respectively. Figure 1a shows the Köhler curve

$f(R) = (A/R) - (B/R^3)$. The peak of the curve is at $R_c = (3B/A)^{1/2} =$ 0.677 μm and $S_c = 2A/(3R_c) = 0.107\%$, where R_c is the critical radius and S_c is the critical supersaturation. The curve crosses the horizontal axis at $R_{eq} = (B/A)^{1/2} = 0.391$ μm, which is the equilibrium radius for the supersaturation $S = 0$.

c. Injection and removal of particles

Cloud droplets are injected into the system at a constant rate J_0 with uniform random initial positions, and they are removed from the system randomly following a residence time τ_{res}. The evolution equation for the number density of cloud droplets n_d is written as

$$\frac{\partial n_d}{\partial t} = J_0 - \frac{1}{\tau_{res}} n_d. \tag{36}$$

In the steady state, the two terms on the right side balance and we obtain

$$n_d = J_0 \tau_{res}. \tag{37}$$

We used a fixed value of $\tau_{res} = 580$ s (=9.7 min.) based on the results from the Π-chamber in C16. We changed the injection rate J_0 and conducted experiments with different number densities. The values of J_0 and n_d are summarized in Table 3. Table 3

d. Random force

The force for the velocity field $\mathbf{f}$ in (23) is a solenoidal, Gaussian random variable with a zero mean, representing white noise (Gotoh et al. 2002), and is applied to the low wavenumber band as

$$\langle \mathbf{f}(\mathbf{k},t)\rangle = 0, \tag{38}$$

$$\langle \mathbf{f}(\mathbf{k},t)\mathbf{f}(-\mathbf{k},s)\rangle = \left(\frac{L_{\rm box}}{2\pi}\right)^3 \left(\delta_{ij} - \frac{k_i k_j}{k^2}\right) \frac{F(k)}{4\pi k^2}\delta(t-s), \tag{39}$$

where $P_{ij}(\mathbf{k}) = \delta_{ij} - \frac{k_i k_j}{k^2}$ and $F(k)$ is the spectrum of the random force defined as

$$F(k) = \begin{cases} c_{\rm f} & (1 \le kL_{\rm box} \le 4) \\ 0 & (\text{otherwise}). \end{cases} \tag{40}$$

The value of $c_{\rm f}$ is set to 30 $\mathrm{cm^2 s^{-3}}$ for the small-scale DNS (Run1–Run10), and to 20 $\mathrm{cm^2 s^{-3}}$ for the large-scale DNS (Run11–Run14).

For forces on scalar fields f_θ and f_q in (26) and (27), respectively, we used only f_q and set $f_\theta = 0$. [As long as we consider the supersaturation, it does not matter whether fluctuations arise from the temperature or water vapor mixing ratio. We also conducted simulations with $f_q = 0$ and non-zero f_θ to excite the supersaturation fluctuation, and confirmed that the same result was obtained when the statistics of the supersaturation fluctuation were unchanged]. The force f_q is a Gaussian random variable with zero mean, representing white noise, and applied to the low wavenumber band. The amplitude of f_q is tuned so that the standard deviation of the

supersaturation fluctuation without cloud droplets is $\sigma_{S_0} = 0.014$ at a statistically steady state. This value is obtained from the measurements with the Π-chamber in C16.

e. DNS

We first conduct small-scale DNS (Run1–Run10). The numerical domain is a triply periodic cubic box with sides of length $L_{\rm box} = 12.8$ cm. We numerically integrate the evolution equations (23) (26)–(31) using the second-order Runge-Kutta scheme with time increment $\Delta t = 1.0 \times 10^{-3}$ s. For the spatial discretization of the flow field, we use the pseudo spectral method with $N = 128$ grid points in each dimension and a grid length $\Delta x = L_{\rm box}/N = 1$ mm. The velocity and scalar fields for the droplet position are linearly interpolated, and the same weighting is used to calculate the condensation rate in (34), i.e., the particle in the cell method (PIC).

We conduct two kinds of experiments: those with and without aerosol effects. For experiments without aerosol effects (Run1–Run5 in Table 3), we integrate (31) without the second and third terms on the right side. Cloud droplets are injected into the system with an initial radius $R_0 = 20$ μm, which is sufficiently large that they are removed from the system before their radius becomes smaller than zero. The purpose of these idealized experiments is to check the consistency between the DNS result and the sta-

tistical theory (15)–(17) as a first step. On the other hand, for experiments with aerosol effects (Run6-Run10 in Table 3), we integrate all of equation (31). Injected cloud droplets are initially unactivated and have a radius $R_0 = 0.39$ μm, which is the equilibrium radius for zero supersaturation as shown in Fig. 1. The injection of unactivated cloud droplets is a model for the injection of aerosol particles in the Π-chamber experiment. When the droplet radius is smaller than 200 nm, we integrate (31) with an implicit scheme and use a Newton-Raphson type iterative scheme to determine the radius in the next step (Shima et al. 2009).

Cloud droplets are initially distributed randomly in the domain with radius R_0 and number density given by (37). Before each run, equations (23), (26)–(31) are integrated for a few large-eddy turnover times without condensation, injection or removal of cloud droplets. The period of numerical integration is 4000 s (4 million steps) for the small-scale DNS to obtain a statistically steady state. The turbulence parameters in the statistically steady state are summarized in Table 2. Definitions of the turbulence parameters are given in Appendix C.

We also conduct large-scale DNS (Run11–Run14) to examine the effect of the domain size. The details are provided in Sec. 3.4.

We use the cloud microphysics simulator, which is a DNS model for cloud turbulence developed in previous studies (Gotoh et al. 2016; Saito and Go-

toh 2018; Saito et al. 2018). The supercomputers used in the present study are mostly the K-computer at the Research Organization for Information Science and Technology (RIST) in Kobe and the Fujitsu FX100 installed at Nagoya University. Parallelization of the computer program is described in Saito and Gotoh (2018).

3.3 Results of small-scale DNS

a. Supersaturation fluctuation

Fig. 2

We first investigate the effect of cloud droplets on the supersaturation fluctuation. Figure 2a shows PDFs for the supersaturation fluctuation in statistically steady states for Run1–Run10, and Table 4 summarizes the standard deviation of the supersaturation ($\sigma_{\rm S}$) and $\tau_{\rm c}$ for each experiment. From (5), the theory predicts that σ_S decreases with decreasing $\tau_{\rm c}$. This tendency is confirmed by comparing Fig. 2a and Table 4.

Table 4

Figure 2b is the same as Fig. 2a except that each distribution is normalized by its variance. The PDFs in Fig. 2b collapse onto a single curve (labeled "Theory"), which is a Gaussian distribution with a zero mean and unit variance, confirming that the supersaturation fluctuation is well approximated by the Gaussian distribution. This is consistent with the observations in the Π-chamber by C16 and also with that in atmospheric clouds (Siebert and Shaw 2017).

We next consider the turbulent mixing time $\tau_{\rm t}$. As explained in (2), the statistical theory developed by C16 uses a single timescale $\tau_{\rm t}$ for turbulent mixing. $\tau_{\rm t}$ is assumed to be the Lagrangian autocorrelation time for the turbulent velocity, which is effectively the same as the turbulence large-eddy turnover time (Desai et al. 2018; Pope 2000). This relies on the assumption that the mixing of scalar field is dominated by the large scale velocity fluctuations.

In order to confirm the validity of the above assumption, we conducted the following investigation. The turbulent velocity field mixes scalar fields through the advection terms in the fluctuation equations for temperature (26) and the water vapor mixing ratio (27). Since the equations for the velocity field (23) are not coupled with the scalar fields in the present DNS, the turbulence statistics for the velocity field are independent of the scalar fields. Then, if we can choose a single timescale for $\tau_{\rm t}$, its value should be the same for Run1–Run10 because the turbulence statistics in the velocity field are the same for each of these runs. Substituting the definition $\tau_{\rm s}^{-1} = \tau_{\rm t}^{-1} + \tau_{\rm c}^{-1}$ into (5) and solving for $\tau_{\rm t}$, we have

$$\tau_{\rm t} = \left(\frac{\sigma_{S_0}^2 - \sigma_S^2}{\sigma_S^2} \right) \tau_{\rm c}, \tag{41}$$

so that all of the parameters on the right side can be obtained from experimental results. By substituting $\sigma_{S_0} = 0.014$ and the results for Run1–Run10 into the right side of (41), we estimate the value of $\tau_{\rm t}$ for each run. Fig. 3

Figure 3 shows the estimated $\tau_{\rm t}$ as a function of the phase relaxation time $\tau_{\rm c}$ for Run1–Run10. As shown in the figure, the estimates for $\tau_{\rm t}$ for these runs, with or without the aerosol effects, are grouped closely around a single horizontal line. In view of the fact that $\tau_{\rm c}$ varies by almost two orders of magnitude (from 0.14 s to 9.0 s) among Run1–Run10, this agreement is remarkable, strongly supporting the validity of using a single value for $\tau_{\rm t}$ (By close observation of Fig. 3, we find that for Run1–Run5 the estimated $\tau_{\rm t}$ value becomes larger for smaller $\tau_{\rm c}$, but this trend is weak and we can regard it as a constant to a first approximation).

From the estimation of $\tau_{\rm t}$ in Fig. 3, the average and standard deviation are given by $\tau_{\rm t} = 0.846 \pm 0.021$ s, respectively, hence we have $\tau_{\rm t} \approx 0.85$ s which is indicated by the horizontal line in Fig. 3. Since the large-eddy turnover time $T_{\rm E}$ is 0.58 s (Table 2), the estimated $\tau_{\rm t}$(=0.85 s) is greater than $T_{\rm E}$ by about 50%. However, the estimation at least confirms that the appropriate choice of $\tau_{\rm t}$ is closer to the timescales for the largest velocity fluctuations. This is consistent with the findings of previous DNS studies of cloud turbulence, where it was shown that the turbulence condensation dynamics are mainly determined by the large flow scales (Sardina et al. 2015; Götzfried et al. 2017). In the following analysis, we use $\tau_{\rm t} = 0.85$ s. Using $\tau_{\rm t} = 0.85$ s to calculate the right side of (5), we obtain the theoretical values for σ_S shown in the second column in Table 4.

497 *b. Droplet size distribution: cases without aerosol effects*

Fig. 4

498 We next consider the effect of the supersaturation fluctuation on the
499 droplet size distribution. We begin with cases without aerosol effects,
500 namely, Run1–Run5.

501 From (15), the theory predicts that the PDF of the squared radius (R^2)
502 is a maximum at the size of the injected particles (R_0^2) and has exponentially
503 decaying tails in a statistically steady state. This is confirmed by Fig. 4a,
504 which shows PDFs for R^2 in statistically steady states for Run1–Run5 with
505 semi-log scaling. Each distribution has its maximum at $R_0^2 = 400$ μm^2
506 and linearly decreasing tails in the semi-log plot. The width of the PDF
507 becomes smaller with increasing run number, or for runs with higher number
508 densities of cloud droplets and smaller supersaturation fluctuations (Tables
509 3 and 4). Figure 4b is the same as Fig. 4a but the PDFs are normalized by

$$\hat{\mathrm{P}}(\hat{R}^2) = \beta_1^2 \mathrm{P}(\hat{R}^2), \qquad \hat{R}^2 = \beta_1^2 |R^2 - R_0^2|, \tag{42}$$

510 where β_1^2 is estimated from the DNS results as

$$\beta_1^2 = \sigma_{R^2}/\sqrt{2} \tag{43}$$

511 based on (18). After normalization, all distributions in Fig. 4b collapse
512 onto the theoretical curve labeled "Theory": $\frac{1}{2}\exp(-|\hat{R}^2|)$ from (15).

Fig. 5

513 The collapse of the DNS results onto the theoretical curve can also be
514 obtained from the time evolution. Figure 5a shows the time evolution of

the variance of the squared radius ($\sigma^2_{R^2}$) for Run1–Run5. As predicted from the Langevin theory, and also as shown in previous DNS studies (Sardina et al. 2015; Siewert et al. 2017), $\sigma^2_{R^2}$ grows linearly with time. With the effect of the sink in (11), the evolution of $\sigma^2_{R^2}$ is (see appendix E)

$$\sigma^2_{R^2} = 2D\tau_{\rm res}(1 - {\rm e}^{-t/\tau_{\rm res}}) = 2\beta^4(1 - {\rm e}^{-t/\tau_{\rm res}}). \tag{44}$$

Figure 5b is the same as Fig. 5a but the results are normalized by β_1^4 in (43). All results collapse onto the theoretical curve: $2(1 - {\rm e}^{-t/\tau_{\rm res}})$.

We next consider the time parameter included in the diffusion coefficient. In the statistical theory, the diffusion coefficient D defined in (9) plays the primary role in the broadening effect of the supersaturation fluctuation on the droplet size distribution. The coefficient D includes the time parameter τ_1. As explained in (8)–(10), the C16 result is recovered if we substitute the system timescale $\tau_{\rm s}$ for τ_1. However, from the analogy with Brownian motion, we can infer that τ_1 should be the timescale of the supersaturation fluctuation felt by each cloud droplet, or the Lagrangian autocorrelation time for the supersaturation fluctuation.

In order to check the importance of the Lagrangian autocorrelation time, we conducted an additional experiment. This experiment is the same as Run1 except that each cloud droplet is fixed at the initial position after it is introduced into the numerical domain. As defined in (7), the system timescale $\tau_{\rm s}$ is calculated from $\tau_{\rm t}$ and $\tau_{\rm c}$. The turbulent mixing time $\tau_{\rm t}$ is

independent of the droplet motion and is solely determined by the turbulent velocity statistics in the present DNS as shown in Fig. 3. The phase relaxation time τ_c in (4) is calculated from the number density and mean radius of the cloud droplets, and is not affected by the droplet motion. Thus, τ_s is also independent of the droplet motion. If we rely on $\tau_1 = \tau_s$ in (9), the droplet size distribution should be the same for Run1 and in the additional experiment in a statistically steady state. Fig. 6

Results for Run1 and the additional experiment are compared in Fig. 6. First, PDFs for the supersaturation fluctuation for the two experiments in statistically steady states are compared in Fig. 6a, which shows no significant differences between the two. This result is consistent with the theory (5), because parameters τ_s and τ_t are unchanged. On the other hand, PDFs of R^2 for the two experiments in statistically steady states are compared in Fig. 6b, which shows significantly different results between the two experiments, in particular, the PDF for the additional experiment is narrower than that for Run1.

It is due to the change of the fluctuation timescale felt by cloud droplets that we obtained the narrower size distribution in the additional experiment. When the positions of cloud droplets are fixed, the fluctuation timescale experienced by cloud droplets is Eulerian. Since the scalar is basically Lagrangian invariant for zero diffusivity, the fluctuation timescale for scalars

is usually longer for the Lagrangian timescale than for the Eulerian one. Hence the smaller τ_1 in (9) for the additional experiment and the narrower size distribution. From the above argument, we conclude that the time parameter τ_1 in (9) should be the Lagrangian autocorrelation time for the supersaturation fluctuation, denoted hereinafter as $\tau_{\rm cor}$:

$$\tau_1 = \tau_{\rm cor}. \tag{45}$$

Table 5

Table 5 compares σ_{R^2} for Run1–Run5 with the theory (T0) calculated from (18), where $\tau_{\rm cor}$ is used for the timescale τ_1. T0 shows almost perfect agreement with the DNS results, which supports the validity of the statistical theory.

Even if we use the system timescale $\tau_{\rm s}$ for τ_1 in (18), the theory provides a good estimate for σ_{R^2} in the present DNS, since $\tau_{\rm s}$ is fairly close to $\tau_{\rm cor}$ as shown in Table 5. However, it should be noted that the Lagrangian autocorrelation time $\tau_{\rm cor}$ is greatly affected by the droplet motion in fluid. For example, $\tau_{\rm cor}$ may change if we introduce the droplet inertia and gravity, which are known to cause substantial changes in the Lagrangian motion of relatively large cloud droplets. We discuss this point in Sec. 5.

c. Droplet size distribution: cases with aerosol effects

Fig. 7

We next consider the results of Run6–Run10 which include aerosol effects. Figure 7 shows the time evolution of the radius of one droplet over 80

s along with the supersaturation experienced by that droplet in Run1. Note that these results are obtained after the droplet size distribution attains a statistically steady state (after 4000 s), and "$t' = 0$" in the horizontal axis corresponds to $t = 4000$ s. The supersaturation is relatively negative from t' =0s to 40s, and the droplet radius is smaller than 3μm during this period. On the other hand, the supersaturation is relatively positive from t' =40s to 80s, and the droplet radius keeps growing, until exceeding 6μm. The wall effect originating from the aerosol effects can be clearly seen in Fig. 7 from t' =0s to 40 s. Around $t' = 20$ s, for example, the droplet radius does not become smaller than zero but remains close to the equilibrium radius even when the supersaturation is negative. Fig. 8

We next examine the PDF of R^2 in a statistically steady state. From (20), the theory predicts that the PDF has its maximum around $R^2 = 0$ and an exponentially decaying right tail. This is confirmed by Fig. 8a, which shows the semi-log plot of the PDFs of R^2 for Run6–Run10 in statistically steady states. The PDFs have linearly decreasing right tails on a semi-log scale, and their widths decrease with increasing run number, or for runs with greater number densities of cloud droplets. Figure 8b is the same as Fig. 8a but each distribution is normalized by

$$\hat{\mathrm{P}}(\hat{R}^2) = \beta_2^2 \mathrm{P}(\hat{R}^2), \qquad \hat{R}^2 = \beta_2^{-2} R^2, \tag{46}$$

where β_2^2 is estimated from the experimental results as

$$\beta_2^2 = \sigma_{R^2} \tag{47}$$

based on (22). The curve labeled "Theory" in Fig. 8b indicates the theoretical curve $\exp(-\hat{R}^2)$, onto which all distributions collapse after normalization. Fig. 9

In cloud physics, PDFs of the droplet radius R (or the diameter d) are often used to investigate cloud properties. Figure 9a shows PDFs of the droplet diameters for Run6–Run10 in statistically steady states. From the relationship $\int P(R^2)dR^2 = \int \mathcal{P}(R)dR$, where $P(R^2)$ and $\mathcal{P}(R)$ are PDFs for R^2 and R, respectively, $P(R^2)$ in (20) can be converted to $\mathcal{P}(R)$ as

$$\mathcal{P}(R) = 2\beta^{-2} R \exp\left(-\beta^{-2}R^2\right), \tag{48}$$

which is the Rayleigh distribution. For the droplet diameter ($d = 2R$), the PDF is

$$\mathsf{P}(d) = (2\beta^2)^{-1} d \exp\left[-(4\beta^2)^{-1}d^2\right]. \tag{49}$$

Using this form, we normalize $\mathsf{P}(d)$ as follows:

$$\hat{\mathsf{P}}(\hat{d}) = \beta_2 \mathsf{P}(\hat{d}), \qquad \hat{d} = \beta_2^{-1} d. \tag{50}$$

Figure 9b shows the results for this normalization along with the theoretical curve: $\left(\hat{d}/2\right)\exp(-\hat{d}^2/4)$. Although the normalized distributions collapse

well onto the theoretical curve for $\hat{d} > 0.5$, they deviate significantly from the theory around $\hat{d} = 0$, and have large peaks. These peaks correspond to unactivated cloud droplets with a radius smaller than the critical radius. Deviations are mainly due to differences in the settings used in the theory and the DNS. In the theory, the radius of injected cloud droplets is assumed to be $R_0 = 0$ for simplicity, whereas $R_0 = 0.39$ μm in the present DNS.

Because the mass of the solute dissolved in each cloud droplet is fixed in the present DNS, the size distributions in Fig. 9 suggest that some of these cloud droplets are activated and larger than the critical radius whereas others are not, depending on the local supersaturation experienced by these cloud droplets in the turbulent environment. This is qualitatively consistent with the results of the Π-chamber experiment (see Fig. 3 in Chandrakar et al. 2017).

Table 6

Table 6 compares σ_{R^2} in statistically steady states for Run6–Run10 with the theory (22), which is indicated by "T0". T0 significantly deviates from the DNS results, with deviations greater for experiments with smaller σ_{R^2}. For Run 10, T0 is almost twice as large as the DNS result. Such significant deviations are contrary to the almost perfect agreement obtained for Run1–Run5 in Table 5.

There are two reasons for the above deviations. The first is that the theory (22) does not include the effect of the mean supersaturation. In the

present DNS, cloud droplets are injected into the system with an initial radius $R_0 = 0.39$ μm, attain the size distribution shown in Figs. 8a and 9a, and are removed from the system over a timescale $\tau_{\rm res}$. Thus, cloud droplets are growing in size on average and the mean condensation rate is positive ($\overline{C}_{\rm d} > 0$). From (28) and (29) for the steady state, we have

$$\overline{T} = T_0 + \frac{L_{\rm v}}{c_{\rm p}} \tau_0 \overline{C}_{\rm d}, \tag{51}$$

$$\overline{Q} = Q_0 - \tau_0 \overline{C}_{\rm d}. \tag{52}$$

When $\overline{C}_{\rm d} > 0$, $\overline{T} > T_0$ and $\overline{Q} < Q_0$, leading to the mean supersaturation $\overline{S}$ which is smaller than S_0 ($S_0 = 0\%$ for the present DNS). The mean supersaturations for Run6–Run10 are shown in the sixth column of Table 6. When the effect of the mean supersaturation $\overline{S}$ is taken into account, the Fokker-Planck equation (11) has the following additional drift term:

$$\begin{aligned} & \frac{\partial n(R^2,t)}{\partial t} + 2K_{\rm s}\overline{S}\,\frac{\partial n(R^2,t)}{\partial R^2} \\ = \; & D\frac{\partial^2 n(R^2,t)}{\partial (R^2)^2} - \frac{1}{\tau_{\rm res}} n(R^2,t) + J_0 \delta(R^2 - R_0^2). \end{aligned} \tag{53}$$

Assuming $R_0 = 0$ and under the reflecting wall boundary condition (12), we obtain the same steady state solution as (20), except that β is replaced by β_-, defined as follows:

$$\beta_- = \frac{\beta}{\left(\sqrt{1+\alpha^2} - \alpha\right)^{1/2}}, \tag{54}$$

where β_-^2 is the root of a quadratic equation and

$$\alpha = \left(2K_{\rm s}\overline{S}\right)\sqrt{\tau_{\rm res}/(4D)}. \tag{55}$$

Using β_-, the variance of the squared radius is

$$\sigma_{R^2}^2 = \beta_-^4 = \beta^4\left[\sqrt{1+\alpha^2}-\alpha\right]^{-2}. \tag{56}$$

Since $\alpha < 0$ for $\overline{S} < 0$, the effect of the negative mean supersaturation is to make $\sigma_{R^2}^2$ smaller. The theoretical values calculated from (56) are shown in the fourth column (T1) in Table 6. Although T1 is closer to the DNS results than T0, there are still significant differences between the theory (T1) and the DNS results.

The second reason for the above deviation is the over-simplification of the aerosol effects in the statistical theory. As explained in (12), one effect of the Köhler equation with solute is to make the droplet radius greater than zero. In addition, another effect is to make the effective supersaturation for droplet growth smaller than S. Figure 1a is reproduced in Fig. 1b on the semi-log scale, and shows that the Köhler curve for the present study is positive and typically has a magnitude of $10^{-2}\%$ for R smaller than 15μm. From (31), the positive value of the Köhler curve effectively acts as negative supersaturation on the cloud droplets. In order to include this effect in a simple way, we approximate the Köhler curve with a single value of $10^{-2}\%$, and replace $\overline{S}$ in (53) with $\left(\overline{S}-S_{\rm K}\right)$, where $S_{\rm K} = 10^{-4}$. The choice of

$S_{\rm K} = 10^{-4}$ is based on Fig. 9a, which shows that most of the cloud droplets in the present DNS are smaller than $R = 15\mu$m ($d = 30$ μm). Theoretical values with the above correction are shown in the fifth column of Table 6 (T2). Although this approximation is crude, with it we obtain fairly close agreement between the theory (T2) and the DNS results.

3.4 Results of large-scale DNS

The results of the small-scale DNS described above show good agreement with the theory. However, the droplet size distributions shown in Fig. 9a are significantly narrower than the results of the Π-chamber experiment. For example, for Run 6 in the present study, the droplets have a number density of 80 cm^{-3} (Table 3), which is close to the cloud droplet number density for the experiment "$\dot{n}_a = 2/cm^3/min$" by C16 as shown in their Table 1. Comparing our size distribution in Fig. 9a with that by C16 in their Fig. 2, the latter is much broader, reaching its tail well beyond a diameter of 30 μm.

Based on the theory, (20) and (54), we can infer two possible reasons for the above discrepancy: the mean supersaturation ($\overline{S}$) and the Lagrangian autocorrelation time for the supersaturation fluctuation ($\tau_{\rm cor}$). First, if $\overline{S}$ is greater than that in the present DNS, the denominator in (54) becomes smaller, resulting in a larger β_- and a broader size distribution. Second, if

$\tau_{\rm cor}$ in (45) is greater than that in the present DNS, the diffusion coefficient D in (9) becomes larger and α in (54) becomes smaller, both resulting in a larger β_- and a broader size distribution.

However, it is not easy to determine the relative importance of $\overline{S}$ and $\tau_{\rm cor}$. For the mean supersaturation $\overline{S}$, the measurements from the Π-chamber by Niedermeier et al. (2018) demonstrate that $\overline{S}$ decreases from ∼2% to almost 0% after the injection of aerosol particles, suggesting that it is difficult to keep $\overline{S}$ positive in the chamber interior. However, this measurement is from an experiment with a relatively high number density of particles ($\sim$ 1200 cm^{-3}), and values of $\overline{S}$ for experiments with lower number densities of particles are unknown. For the Lagrangian autocorrelation time $\tau_{\rm cor}$, $\tau_{\rm cor}$ is expected to be closely related to the turbulence statistics and the spatio-temporal scale of the largest eddies (Tennekes and Lumley 1972). Turbulence statistics for the Π-chamber experiment are given in Chang et al. (2016) (see their Table 3), who estimated that η=0.11cm, λ=1.6cm, $\mathcal{L}$ = 8.8cm, and R_λ = 55. These estimates are fairly close to the corresponding turbulence statistics for the small-scale DNS in the present study (See Table 2). However, we should keep in mind the difficulty in measuring the turbulence statistics in the Π-chamber where, unlike a wind-tunnel experiment, there is no mean flow and hence Taylor's hypothesis of frozen turbulence does not necessarily hold.

Given the uncertainties in the measurements of the mean supersaturation $\overline{S}$ and the turbulence statistics described above, we have to simplify the question so that the problem can be addressed by the present DNS. Because the effect of $\overline{S}$ for the droplet growth is well known, and also, as described in the previous subsection, $\overline{S}$ in the present DNS is affected by the nudging parameter τ_0, the choice of which is largely arbitrary, here we focus on the effect of turbulence and consider the following question: if we make the domain and corresponding largest possible eddy size comparable to those for the Π-chamber, can the broadening effect of the supersaturation fluctuation in the present DNS explain the droplet size distributions in the Π-chamber?

In order to answer this question, we conducted the following large-scale DNS: Run11-Run14. The setups for these experiments are the same as those for Run6–Run10 except the box length is $L_{\rm box} = 102.4$cm, the grid number is $N = 512$ in each dimension, the grid length is $\Delta x = 2$mm, the time increment is $\Delta t = 0.8 \times 10^{-3}$ s, the nudging time is $\tau_0 = 2$ s in (28) and (29), and the parameters shown in Table 3 are used. The turbulence parameters for Run11–Run14 are shown in Table 2. The period of numerical integration is 3600 s (4.5 million steps) in order for the large-scale DNS to obtain a statistically steady state.

Fig. 10

Figure 10 shows PDFs of the droplet diameter in statistically steady

states for Run11–Run14. In comparison to the results of the small-scale DNS in Fig. 9a, the distributions in Fig. 10 are broader (compare Run7 and Run12, which have almost the same number density of $\sim$ 80 cm^{-3}). Furthermore, the number densities for Run11–Run13 approximately correspond to the cloud droplet number densities for the "$\dot{n}_a = 1, 2, 4/cm^3/min$" experiments in C16, respectively. The results shown in their Fig. 2 and our Fig. 10, seem to agree quantitatively. Fig. 11

Figure 11 shows the spectra for the kinetic energy and the variance of the supersaturation for the large-scale DNS. Since the Taylor microscale Reynolds number R_λ is 207, a wavenumber range with a slope close to -5/3 can be seen in the middle of these spectra. These results are consistent with the power spectral density for the vertical velocity fluctuations measured in the Π-chamber (see Fig.8 in Chang et al. 2016), but again the difficulties in measuring the turbulence statistics in the Π-chamber should be noted. Table 7

Table 7 shows the standard deviation of the supersaturation (σ_S) for the large-scale DNS. By substituting the results for Run11–Run14 into the right side of (41), the turbulent mixing time for the large-scale DNS is estimated as $\tau_\mathrm{t} = 3.824 \pm 0.173 \approx 3.82$ s, which is about 70% greater than the large-eddy turnover time ($T_\mathrm{E} = 2.2$ s, see Table 2). This again confirms that the correct value of τ_t is of the same order as T_E, but also indicates the possibility that the ratio $\tau_\mathrm{t}/T_\mathrm{E}$ weakly depends on the domain size and

other turbulence parameters such as the Reynolds number.

Table 8 shows the standard deviation of the squared radius (σ_{R^2}) for the large-scale DNS. Values of $\tau_{\rm cor}$ are over 1 s, which are at least twice as large as $\tau_{\rm cor}$ for the small-scale DNS (see Table 6). Accordingly, the diffusion coefficients (D) for the large-scale DNS are larger in (9), resulting in the broader size distributions as shown in Fig. 10. The experimental results for σ_{R^2} seem to agree fairly well with the theoretical results (T2) in Table 8. Table 8

4. Discussion

The results in the present study are very satisfactory and encouraging for the future research of cloud and turbulence using the cloud microphysics simulator. At the same time, however, we should note several important differences between the present study and atmospheric clouds and turbulence. As described in Sec. 1, the main purpose of the present study was to compare our DNS results with the statistical theory and the laboratory experiment by C16. Since there are differences in the physical parameters and conditions of the atmospheric clouds and the laboratory clouds in the Π-chamber, the interpretation of the present results in the context of the atmospheric clouds needs great care. Among those points, important ones are as follows:

1. *Time scale of turbulence.* The interaction between the supersatura-

763 tion fluctuation and cloud droplets substantially depends on the ratio be-
764 tween the phase relaxation time $\tau_{\rm c}$ and the turbulence large-eddy turnover
765 time $T_{\rm E}$, that is, the Damköhler number: Da $= T_{\rm E}/\tau_{\rm c}$. The large eddy
766 turnover time T_E tends to increase with the Reynolds number. For ex-
767 ample, $T_{\rm E}$ is of the order of several tens of seconds in atmospheric clouds
768 at $R_\lambda \approx 5000$ (Siebert and Shaw 2017), while it is shorter than several
769 seconds in the present DNS at $R_\lambda \approx 200$ and the Π-chamber experiment.
770 The dumping effect of cloud droplets on the supersaturation fluctuation in-
771 creases with the Reynolds number and thus more significant in atmospheric
772 clouds [see Eq. (5)], which in turn affects the droplet growth by condensa-
773 tion/evaporation.

774 2. *Mean supersaturation.* In the present DNS, the mean supersaturation
775 is kept close to a statistically steady value [$=S_0(T_0, Q_0)$] by nudging terms
776 in (28) and (29), and we set $S_0(T_0, Q_0) = 0$ for simplicity. In atmospheric
777 clouds, however, droplet size distributions form in updrafts and associated
778 mean supersaturation due to adiabatic cooling, when diffusion growth of
779 droplet takes place. Because the positive mean supersaturation has the
780 effect of narrowing the PDF of the droplet radius (not the squared radius) in
781 ascending adiabatic volume (see Grabowski and Wang 2013, and references
782 therein), the effect of the mean supersaturation should be taken into account
783 when investigating the formation mechanism of the droplet size distribution

in atmospheric clouds.

Note that the cloud microphysics simulator can incorporate the mean supersaturation effects, for example, by ascending the cubic box with updraft velocity that is self-consistently determined through the buoyancy force. Indeed the narrowing of the PDF of the droplet radius has successfully been simulated, showing that the cloud microphyiscs simulator is able to compute complex nonlinear interaction between mean and fluctuations (Saito and Gotoh, 2018). For the future studies of the cloud microphysics, however, it is necessary to verify the code and indispensable to obtain deeper understanding of the effects of the supersaturation fluctuation. As a simple but most effective way for this purpose, we compared the results of the cloud microphysics simulator with the experimental results by C16. The good agreement obtained in the present study is very encouraging for the future application of the cloud microphysics simulator.

3. *Generation mechanism for supersaturation fluctuation.* Fluctuations of supersaturation in atmospheric clouds are considered to be correlated with fluctuations of vertical velocity. On the other hand, in the present DNS, we used the external scalar injections that are not correlated with the corresponding forces of the velocity field (see Sec. 3.2). One way to model the excitation of the supersaturation fluctuation which is correlated with the vertical velocity field is to use the scalar injection Γu_z, propor-

tional to the vertical velocity u_z times the prescribed vertical scalar mean gradient Γ (Gotoh and Watanabe 2015). Such kind of scalar injections are often used in DNS studies on cloud turbulence (Celani et al. 2005; Lanotte et al. 2009; Sardina et al. 2015; Saito and Gotoh 2018), while several other studies use the same kind of forces as the present study (Siewert et al. 2017). It is easily found that the dimensional estimate for the scalar injection in the wavenumber space yields $F_\theta(k) \propto \Gamma^2 \tau(k) E(k) \propto k^{-7/3}$, where $\tau(k) (\propto k^{-2/3})$ and $E(k) (\propto k^{-5/3})$ are the characteristic time and the kinetic energy spectrum of turbulence in the inertial range, respectively. Therefore it follows that the scalar injection proportional to the vertical velocity has most inputs at very low wavenumbers, which means that there are no difference in effects between the low wavenumber injection and the injection proportional to the vertical velocity. Indeed the low order moments such as the spectrum of the scalar variances and Yaglom's 4/3 laws obtained by simulations using two different injections are the same (Gotoh and Yeung 2013; Saito and Gotoh 2018). The above arguments and facts support the suggestion by Siewert et al. (2017) that the properties of the supersaturation field without droplets are expected to be insensitive to the specific form of the scalar injection.

5. Summary

The purpose of the present study was to conduct direct numerical simulations (DNSs) of the growth of cloud droplets by condensation in turbulence using our DNS model "cloud microphysics simulator", and to compare the results with the statistical theory proposed by Chandrakar et al. (2016) (referred to as "C16") and the experimental results from their laboratory cloud chamber, the "Π-chamber". For this purpose, we first made several extensions to the statistical theory by C16. We derived the Fokker-Planck equation for the droplet size distribution and introduced aerosol (curvature and solute) effects into the equation with a zero flux boundary condition, which is mathematically equivalent to the case of Brownian motion in the presence of a wall. We obtained an analytical expression for the size distribution in a steady state which is proportional to $R\exp(-cR^2)$, where c is a constant. Next, we conducted a small-scale DNS ($L_{\rm box} = 12.8$cm) and showed that the results agree closely with the theory. In addition, by careful analysis of the DNS data, we found that the proper value for the turbulent mixing time ($\tau_{\rm t}$) in the theory is greater than the large-eddy turnover time for turbulence by about 50%. We also found that the diffusion coefficient in the Fokker-Planck equation should be expressed in terms of the Lagrangian autocorrelation time for the supersaturation fluctuation. Finally, we conducted a large-scale DNS ($L_{\rm box} = 102.4$cm) with a domain size comparable

to the size of the Π-chamber, and obtained steady state size distributions which are quantitatively consistent with the results of the Π-chamber experiment.

As described in Sec. 3, there are many processes that are not included in the present DNS for simplicity, such as particle inertia, gravity, collision-coalescence and buoyancy. Nevertheless, it is still remarkable that quantitatively consistent results are obtained among the large-scale DNS, the statistical theory, and the Π-chamber experiment, suggesting that these share the essence of the formation mechanism of the droplet size distribution by condensation in turbulence. This agreement provides validation for our DNS and encourages further studies in this direction.

For future studies, we should clarify the effects of the simplifications in the present DNS. First, while the Π-chamber has solid boundaries and excites turbulence by moist Rayleigh-Benard convection, the present DNS assumed a periodic domain and excited turbulence by random external forces. The effects of these simplifications can be investigated by DNSs or large-eddy simulations of moist Rayleigh-Benard convection with more realistic boundary conditions.

Second, the present DNS neglected particle inertia and gravity. Because these processes are known to cause substantial changes in particle trajectories especially for larger particles (Sundaram and Collins 1997; Falkovich

and Pumir 2007), these changes can in turn affect the Lagrangian autocorrelation time for the supersaturation fluctuation $\tau_{\rm cor}$. In fact, Vaillancourt et al. (2002) reported that the gravitational sedimentation reduces the broadening effect of the supersaturation fluctuation on the droplet size distribution. Clarifying the effects of particle inertia and gravity on the correlation time could also be useful for informing cloud microphysical parameterizations proposed in recent studies (Grabowski and Abade 2017; Sardina et al. 2018).

Third, to facilitate the comparison with the statistical theory, the present DNS assumed that the particle removal process is independent of the particle size so that the residence timescale $\tau_{\rm res}$ is constant. However, since particles in the Π-chamber are removed by gravitational sedimentation, $\tau_{\rm res}$ is expected to be shorter for larger particles. A possible effect of a shorter $\tau_{\rm res}$ for larger particles was reported in the Π-chamber experiment by C16. The effect of gravity could also change the functional form of the steady state size distribution obtained from the Fokker-Planck equation in Sec. 2, thereby changing the statistical properties of the distribution. Full scale simulation including those effects is really challenging and will be reported somewhere.

Acknowledgements

We are grateful to Dr. Kamal Kant Chandrakar, Prof. Raymond Shaw, and Prof. Will Cantrell for fruitful discussions and instructive comments. We are also grateful to two anonymous reviewers for many useful comments. I.S. is also grateful to Dr. Yuki Yasuda and Prof. Keiichi Ishioka for encouraging comments. This research used computational resources of the K computer provided by the RIKEN Center for Computational Science through the HPCI System Research project (Project ID: hp170189, hp180070). The computational supports provided by the Japan High Performance Computing and Networking, Large-scale Data Analyzing and Information Systems (JHPCN) (jh170013, jh180009), the High Performance Computing (HPC 2017, 2018) at Nagoya University and the Earth Simulator supercomputer system operated by the Japan Agency for Marine-Earth Science and Technology (JAMSTEC) are also gratefully acknowledged. This work was supported by MEXT KAKENHI through Grant No. 15H02218 and JSPS KAKENHI Grants No. 18K03925 and No. 18K13611.

Appendix A: Phase relaxation time τ_c

The phase relaxation time τ_c is introduced by Cooper (1989). The derivation of τ_c is explained in Lanotte et al. (2009) (see also Sardina

et al. 2015; Kumar et al. 2013). $\tau_{\rm c}$ is given as follows:

$$\tau_{\rm c}^{-1} = 4\pi K_{\rm s}\frac{\rho_{\rm w}}{\rho_{\rm a}}\left(\frac{1}{Q_{\rm vs}} + \frac{\varepsilon_0 L_{\rm v}^2}{c_{\rm p}R_{\rm d}T^2}\right) n_{\rm d}\overline{R} \quad \left(\propto n_{\rm d}\overline{R}\right). \tag{57}$$

Here, the saturation mixing ratio $Q_{\rm vs}$ is given by (33). With $T = 290$ K and the parameters taking the values shown in Table 1, Eq. (57) gives

$$\tau_{\rm c}^{-1} = 2.776...[{\rm cm^2 s^{-1}}] \times n_{\rm d}\overline{R}. \tag{58}$$

This equation is used to estimate $\tau_{\rm c}$ in the present study.

Appendix B: Parameters for Köhler curve

For a drop of a sufficiently dilute aqueous solution, A and B in (31) are given as follows (Pruppacher and Klett 1997):

$$A = \frac{2M_{\rm w}\sigma_{\rm w}}{R_{\rm g}\rho_w T_A} \tag{59}$$

$$B = \frac{3\nu_{\rm s}\Phi_{\rm s}m_{\rm s}M_{\rm w}}{4\pi M_{\rm s}\rho_{\rm w}}, \tag{60}$$

where T_A is the temperature around a drop. We set T_A as a constant because the temperature change in the present DNS is sufficiently small. Definitions of the other parameters in (59) and (60) are given in Tables 1 and 9.

We assume that the solute dissolved in each drop is NaCl (sodium chloride) with a fixed mass of $m_{\rm s} = 1.13 \times 10^{-15}$ g. This value of $m_{\rm s}$ corresponds to a sphere with a 50 nm radius and a density $\rho_{\rm s} = 2.16$ g cm^{-3}.

Substituting the parameters in Tables 1 and 9 into (59) and (60), we obtain $A = 1.089 \times 10^{-7}$ cm and $B = 1.665 \times 10^{-16}$ cm^3, respectively. Table 9

Appendix C: Definitions of turbulence parameters

The kinetic energy is defined by

$$E = \frac{1}{2}\langle u_i^2 \rangle = \int_0^\infty E(k)dk, \tag{61}$$

where u_i $(i = 1, 2, 3)$ are components of the velocity vector $\mathbf{u}$ (repeated indices are summed), the angle brackets $\langle \cdots \rangle$ represent the spatial and temporal averages, and $E(k)$ is the kinetic energy spectrum. The mean energy dissipation rate is defined by

$$\epsilon = \frac{\nu_\mathrm{a}}{2}\langle (\partial_i u_j + \partial_j u_i)^2 \rangle. \tag{62}$$

The integral scale, Taylor microscale, and Kolmogorov scale are respectively defined by

$$\mathcal{L} = \left(\frac{3\pi}{4E}\right)\int_0^\infty k^{-1}E(k)dk \tag{63}$$

$$\lambda = \sqrt{\langle u_1^2 \rangle / \langle (\partial_1 u_1)^2 \rangle} \tag{64}$$

$$\eta_\mathrm{K} = \left(\nu_\mathrm{a}^3/\epsilon\right)^{1/4}. \tag{65}$$

The large-eddy turnover time and Kolmogorov time are respectively defined by

$$T_\mathrm{E} = \mathcal{L}/u_\mathrm{rms} \tag{66}$$

$$\tau_{\rm K} \;=\; (\nu_{\rm a}/\epsilon)^{1/2}, \tag{67}$$

where $u_{\rm rms} = \sqrt{2E/3}$ is the root-mean-square velocity. The Taylor microscale Reynolds number is defined by

$$R_\lambda = u_{\rm rms}\lambda/\nu_{\rm a}. \tag{68}$$

Appendix D: Statistical properties of the size distribution

The functional forms of the PDFs of R and R^2 are given in (20) and (48), respectively. The statistical properties of the size distribution are as follows. The mean radius:

$$\overline{R} = \int_0^\infty R\,\mathcal{P}(R)dR = \frac{\sqrt{\pi}}{2}\beta. \tag{69}$$

The mean squared radius is given in (21) and $\overline{R^2} = \beta^2$. The mean cubic radius:

$$\overline{R^3} = \int_0^\infty R^3\,\mathcal{P}(R)dR = \frac{3\sqrt{\pi}}{4}\beta^3. \tag{70}$$

The variance of R:

$$\sigma_R^2 = \overline{R^2} - \left(\overline{R}\right)^2 = \frac{(4-\pi)}{4}\beta^2. \tag{71}$$

The variance of R^2 is given in (22) and $\sigma_{R^2}^2 = \beta^4$. The relative dispersion:

$$\frac{\sigma_R}{\overline{R}} = \sqrt{\frac{4-\pi}{\pi}} = 0.5227... \approx 0.52. \tag{72}$$

The relative dispersion measured in the Π-chamber is between 0.2 and 0.4 (Desai et al. 2018; Chandrakar et al. 2018b). The mean volume radius:

$$R_{\mathrm{v}} = \left(\overline{R^3}\right)^{1/3} = \left(\frac{3\sqrt{\pi}}{4}\right)^{1/3} \beta \tag{73}$$

The effective radius:

$$R_{\mathrm{e}} = \frac{\overline{R^3}}{\overline{R^2}} = \frac{3\sqrt{\pi}}{4}\beta. \tag{74}$$

The parameter k used in cloud physics is given by

$$k = \frac{R_{\mathrm{v}}^3}{R_{\mathrm{e}}^3} = \left(\frac{3\sqrt{\pi}}{4}\right)^{-2} = 0.5658... \approx 0.57 \tag{75}$$

(For details of the parameter k, readers are referred to Martin et al. 1994; Chandrakar et al. 2018a) $k = 0.80 \pm 0.07$ for maritime airmass clouds and $k = 0.67 \pm 0.07$ for continental airmass clouds (Martin et al. 1994). $k = 0.66 \pm 0.01$ for the Π-chamber (Chandrakar et al. 2018a).

Appendix E: Solution of the Fokker-Planck equation

Here we consider the solution to the Fokker-Planck equation (11) with the boundary conditions (12) and (13), and the initial conditions (14) (Chandrasekhar 1943). The analytical solution is expressed in terms of Green's function as

$$n(\rho, t) = e^{-t/\tau_{\mathrm{res}}} \int_0^\infty G(\rho, \rho') n_0(\rho') d\rho' + J_0 \int_0^t e^{-s/\tau_{\mathrm{res}}} G(\rho, \rho_0, s) ds, \tag{76}$$

$$G(\rho, \rho', t) = \frac{1}{\sqrt{4\pi D t}} \left[\exp\left(-\frac{(\rho - \rho')^2}{4Dt}\right) + \exp\left(-\frac{(\rho + \rho')^2}{4Dt}\right) \right] H(t), \tag{77}$$

where $\rho = R^2 \geq 0$ for ease of writing and $H(t)$ is the Heaviside function. It is readily found that G satisfies the boundary condition $\partial G(\rho, \rho', t)/\partial \rho = 0$ at $\rho = 0$ and the normalization

$$\int_0^\infty G(\rho, \rho', t) d\rho = H(t). \tag{78}$$

The first term of the right hand side of Eq.(76) arises from the initial condition of n which decays in time. Integration of $n(\rho, t)$ over ρ yields the number density $n_{\rm d}(t)$ as function of time as

$$n_{\rm d}(t) = n_{\rm d0} e^{-t/\tau_{\rm res}} + J_0 \tau_{\rm res} \left(1 - e^{-t/\tau_{\rm res}}\right). \tag{79}$$

where $n_{\rm d0}$ is the initial number density. The probability density function $P(\rho, t)$ is given by

$$P(\rho, t) d\rho = \frac{n(\rho, t) d\rho}{n_{\rm d}(t)}. \tag{80}$$

In order to make the arguments simpler we put

$$n(\rho, 0) = n_{\rm d0} \delta(\rho - \rho_0), \tag{81}$$

so that the probability density function (PDF) $P(\rho, t)$ at latter times is given by

$$P(\rho, t) = \frac{1}{n_{\rm d}(t)} \left[n_{\rm d0} e^{-t/\tau_{\rm res}} G(\rho, \rho_0, t) + J_0 \int_0^t e^{-s/\tau_{\rm res}} G(\rho, \rho_0, s) ds \right]. \tag{82}$$

Now we consider two cases. First let $\rho_* = R_*^2$ be the square of the droplet radius at which the Köhler curve attains the maximum.

Case 1 $\rho_* \ll |\rho - \rho_0| \sim \sqrt{D\tau_{\rm res}} \ll \rho_0$.

This corresponds to the domain of droplet radius in which the aerosol effects are negligible. Writing as $\rho_0 - \rho = \xi$ we have the estimate $(\rho + \rho_0)^2 = 4\rho_0^2\,(1 - (\xi/\rho_0) + (\xi/\rho)^2/4) \sim 4\rho_0^2$. Then the second term of the right hand side of Eq.(77) becomes negligible compared to the first term, and thus the PDF is approximately

$$P(\rho,t) \;=\; \frac{1}{n_{\rm d}(t)\sqrt{4\pi D}}\left[n_{\rm d0}\frac{1}{\sqrt{t}}\exp\left(-\frac{t}{\tau_{\rm res}} - \frac{(\rho-\rho_0)^2}{4Dt}\right)\right.$$
$$\left. +J_0\int_0^t \frac{1}{\sqrt{s}}\exp\left(-\frac{s}{\tau_{\rm res}} - \frac{(\rho-\rho_0)^2}{4Ds}\right)ds\right]. \qquad (83)$$

At latter times as $t \gg \tau_{\rm res}$ the contribution from the initial condition (the first term) vanishes and the second integral reduces to

$$P_\infty(\rho) = \frac{1}{\sqrt{4D\tau_{\rm res}}}\exp\left(-\frac{|\rho-\rho_0|}{\sqrt{D\tau_{\rm res}}}\right), \qquad (84)$$

which is Eq.(15). Here we used the formula

$$\int_0^\infty \exp\left(-ax^2 - \frac{b}{x^2}\right)dx = \frac{1}{2}\sqrt{\frac{\pi}{a}}\exp\left(-2\sqrt{ab}\right). \qquad (85)$$

The moments $M_n(t) = \overline{[\rho(t)]^n}$ are computed by the standard way as

$$M_n(t) \;=\; \int_0^\infty \rho^n P(\rho,t)d\rho$$
$$= \frac{1}{n_{\rm d}(t)\sqrt{4\pi D}}\left[n_{\rm d0}\frac{1}{\sqrt{t}}e^{-t/\tau_{\rm res}}\int_{-\rho_0}^\infty(\rho_0+\xi)^n\exp\left(-\frac{\xi^2}{4Dt}\right)d\xi\right.$$
$$\left. +J_0\int_0^t\frac{1}{\sqrt{s}}e^{-s/\tau_{\rm res}}\int_{-\rho_0}^\infty(\rho_0+\xi)^n\exp\left(-\frac{\xi^2}{4Ds}\right)d\xi\;ds\right]. \qquad (86)$$

The lower boundary $-\rho_0$ of the integral can effectively be replaced by $-\infty$ because of $\sqrt{Dt} \ll \rho_0$ in the present case. We obtain the mean and the variance as

$$\begin{aligned} \overline{\rho(t)} &= \rho_0, \qquad (87) \\ \sigma^2(t) &= \overline{[\rho(t)]^2} - \overline{\rho(t)}^2 \\ &= 2D\tau_{\rm res}\frac{J_0\tau_{\rm res}}{n_{\rm d}(t)}\left[1-\left(1+\left(1-\frac{n_{\rm d0}}{J_0\tau_{\rm res}}\right)\frac{t}{\tau_{\rm res}}\right)e^{-t/\tau_{\rm res}}\right] \qquad (88) \\ &\to 2D\tau_{\rm res} \quad \text{as} \quad t\to\infty. \end{aligned}$$

The mean value is independent of time and the variance approaches the constant $2D\tau_{\rm res}$ at large t. When $\frac{n_{\rm d0}}{J_0\tau_{\rm res}} = 1$, Eq.(88) reduces to Eq.(44).

Case 2 $\rho_* \sim \rho_0$.

This corresponds to the domain of small droplets so that the aerosols affect the distribution function at very small radius. Simple analytical expression of the PDF for all time is not available, and the precise functional form may be obtained by numerical integration of Eq.(82). However, when we focus on the asymptotic state at large time, the asymptotic PDF can be obtained. The first term (the initial contribution) of the right hand side of Eq.(82) vanishes and the second term is

$$\begin{aligned} P(\rho) &= \frac{1}{\sqrt{4\pi D\tau_{\rm res}}}\int_0^\infty \frac{1}{\sqrt{s}}e^{-s/\tau_{\rm res}}\left[\exp\left(-\frac{(\rho-\rho_0)^2}{\sqrt{4Ds}}\right)+\exp\left(-\frac{(\rho+\rho_0)^2}{\sqrt{4Ds}}\right)\right]ds \\ &= \frac{1}{\sqrt{4D\tau_{\rm res}}}\left[\exp\left(-\frac{|\rho-\rho_0|}{\sqrt{D\tau_{\rm res}}}\right)+\exp\left(-\frac{|\rho+\rho_0|}{\sqrt{D\tau_{\rm res}}}\right)\right]. \qquad (89) \end{aligned}$$

At $\rho \ll \rho_*$ the PDF is

$$P(\rho = 0) = \frac{1}{\sqrt{D\tau_{\rm res}}} \exp\left(-\frac{\rho_0}{\sqrt{D\tau_{\rm res}}}\right), \tag{90}$$

and for large $\rho \gg \rho_* \sim \rho_0$

$$P(\rho) = \frac{1}{\sqrt{D\tau_{\rm res}}} \exp\left(-\frac{\rho}{\sqrt{D\tau_{\rm res}}}\right). \tag{91}$$

The mean and variance at large time are

$$\begin{aligned} \overline{\rho} &= \rho_0 + \sqrt{D\tau_{\rm res}} e^{-\rho_0/\tau_{\rm res}} && (92) \\ &\to \sqrt{D\tau_{\rm res}} \quad \text{for} \quad \rho_0 \to 0 \\ \sigma^2(t) &= D\tau_{\rm res}\left(2 - e^{-2\rho_0/\sqrt{D\tau_{\rm res}}} - 2\frac{\rho_0}{\sqrt{D\tau_{\rm res}}} e^{-\rho_0/\sqrt{D\tau_{\rm res}}}\right) && (93) \\ &\to D\tau_{\rm res} \quad \text{for} \quad \rho_0 \to 0 \end{aligned}$$

respectively, and they are Eqs. (21) and (22), respectively.

References

Ayala, O., B. Rosa, and L.-P. Wang, 2008a: Effects of turbulence on the geometric collision rate of sedimenting droplets. Part 2. Theory and parameterization. *New J. Phys.*, **10**, 075016.

Ayala, O., B. Rosa, L.-P. Wang, and W. W. Grabowski, 2008b: Effects of turbulence on the geometric collision rate of sedimenting droplets:

1001 Part 1. Results from direct numerical simulation. *New J. Phys.*, **10**,
1002 075015.

1003 Bodenschatz, E., 2015: Clouds resolved. *Science*, **350**, 40–41.

1004 Bodenschatz, E., S. P. Malinowski, R. A. Shaw, and F. Stratmann, 2010:
1005 Can we understand clouds without turbulence? *Science*, **327**, 970–
1006 971.

1007 Celani, A., G. Falkovich, A. Mazzino, and A. Seminara, 2005: Turbulent
1008 condensation of droplets: Direct simulation and a stochastic model.
1009 *Europhys. Lett.*, **66**, 723–740.

1010 Celani, A., A. Mazzino, and M. Tizzi, 2009: Droplet feedback on vapor in
1011 a warm cloud. *Int. J. Mod. Phys.*, **23**, 5434–5443.

1012 Chandrakar, K. K., W. Cantrell, K. Chang, D. Ciochetto, D. Niedermeier,
1013 M. Ovchinnikov, R. A. Shaw, and F. Yang, 2016: Aerosol indirect
1014 effect from turbulence-induced broadening of cloud-droplet size dis-
1015 tributions. *Proc. Nat. Acad. Sci.*, **113**, 14243–14248.

1016 Chandrakar, K. K., W. Cantrell, D. Ciochetto, S. Karki, G. Kinney, and
1017 R. A. Shaw, 2017: Aerosol removal and cloud collapse accelerated by
1018 supersaturation fluctuations in turbulence. *Geophys. Res. Lett.*, **44**,
1019 4359–4367.

1020 Chandrakar, K. K., W. Cantrell, A. B. Kostinski, and R. A. Shaw, 2018a:
1021 Dispersion aerosol indirect effect in turbulent clouds: Laboratory
1022 measurements of effective radius. *Geophys. Res. Lett.*, **45**, 10738–
1023 10745.

1024 Chandrakar, K. K., W. Cantrell, and R. A. Shaw, 2018b: Influence of turbu-
1025 lent fluctuations on cloud droplet size dispersion and aerosol indirect
1026 effects. *J. Atmos. Sci.*, **75**, 3191–3209.

1027 Chandrasekhar, S., 1943: Stochastic problems in physics and astronomy.
1028 *Rev. Mod. Phys.*, **15**, 1–89.

1029 Chang, K., J. Bench, M. Brege, W. Cantrell, K. K. Chandrakar, D. Cio-
1030 chetto, C. Mazzoleni, L. R. Mazzoleni, D. Niedermeier, and R. A.
1031 Shaw, 2016: A laboratory facility to study gas-aerosol-cloud inter-
1032 actions in a turbulent environment: The π chamber. *Bull. Amer.*
1033 *Meteor. Soc.*, **97**, 2343–2358.

1034 Chen, S., M.-K. Yau, and P. Bartello, 2018a: Turbulence effects of colli-
1035 sion efficiency and broadening of droplet size distribution in cumulus
1036 clouds. *J. Atmos. Sci.*, **75**, 203–217.

1037 Chen, S., M.-K. Yau, P. Bartello, and L. Xue, 2018b: Bridging the
1038 condensation-collision size gap: a direct numerical simulation of con-

1039 tinuous droplet growth in turbulent clouds. *Atmos. Chem. Phys.*,
1040 **18**, 7251–7262.

1041 Clark, T. L., and W. D. Hall, 1979: A numerical experiment on stochastic
1042 condensation theory. *J. Atmos. Sci.*, **36**, 470–483.

1043 Cooper, W. A., 1989: Effects of variable droplet growth histories on droplet
1044 size distributions. part I: Theory. *J. Atmos. Sci.*, **46**, 1301–1311.

1045 Davidson, P., Y. Kaneda, and K. Sreenivasan, 2012: *Ten Chapters in Tur-*
1046 *bulence*. Cambridge University Press, 450.

1047 Desai, N., K. K. Chandrakar, K. Chang, W. Cantrell, and R. A. Shaw, 2018:
1048 Influence of microphysicsl variability on stochastic condensation in a
1049 turbulent laboratory cloud. *J. Atmos. Sci.*, **75**, 189–201.

1050 Devenish, B. J., P. Bartello, J.-L. Brenguier, L. R. Collins, W. W.
1051 Grabowski, R. H. A. IJzermans, S. P. Malinowski, M. W. Reeks,
1052 J. C. Vassilicos, L.-P. Wang, and Z. Warhaft, 2012: Droplet growth
1053 in warm turbulent clouds. *Q. J. R. Meteorol. Soc.*, **138**, 1401–1429.

1054 Falkovich, G., and A. Pumir, 2007: Sling effect in collisions of water droplets
1055 in turbulent clouds. *J. Atmos. Sci.*, **64**, 4497–4505.

1056 Franklin, C. N., P. A. Vaillancourt, and M. K. Yau, 2007: Statistics and pa-

rameterizations of the effect of turbulence on the geometric collision kernel of cloud droplets. *J. Atmos. Sci.*, **64**, 938–954.

Franklin, C. N., P. A. Vaillancourt, M. K. Yau, and P. Bartello, 2005: Collision rates of cloud droplets in turbulent flow. *J. Atmos. Sci.*, **62**, 2451–2466.

Frisch, U., 1995: *Turbulence*. Cambridge University Press.

Gotoh, T., D. Fukuyama, and T. Nakano, 2002: Velocity field statistics in homogeneous steady turbulence obtained using a high-resolution direct numerical simulation. *Phys. Fluids*, **14**, 1065–1081.

Gotoh, T., T. Suehiro, and I. Saito, 2016: Continuous growth of cloud droplets in cumulus cloud. *New J. Phys.*, **18**, 043042.

Gotoh, T., and T. Watanabe, 2015: Power and nonpower laws of passive scalar moments convected by isotropic turbulence. *Phys. Rev. Lett.*, **115**, 114502.

Gotoh, T., and P. K. Yeung, 2013: *Ten Chapers in Turbulence*. Cambridge University Press, Cambridge, UK.

Götzfried, P., B. Kumar, R. A. Shaw, and J. Schumacher, 2017: Droplet dynamics and fine-scale structure in a shearless turbulent mixing layer with phase changes. *J. Fluid Mech.*, **452**, 452–483.

1076 Grabowski, W. W., and G. C. Abade, 2017: Broadening of cloud droplet
1077 spectra through eddy hopping: Turbulent adiabatic parcel simula-
1078 tions. *J. Atmos. Sci.*, **74**, 1485–1493.

1079 Grabowski, W. W., and L.-P. Wang, 2009: Diffusional and accretional
1080 growth of water drops in a rising adiabatic parcel: effects of the
1081 turbulent collision kernal. *Atmos. Chem. Phys.*, **9**, 2335–2353.

1082 Grabowski, W. W., and L.-P. Wang, 2013: Growth of cloud droplets in a
1083 turbulent environment. *Annu. Rev. Fluid Mech.*, **45**, 293–324.

1084 Houze, J. R. A., 2014: *Cloud Dynamics* (2 Ed.). Academic Press, 432.

1085 Korolev, A. V., and I. P. Mazin, 2003: Supersaturation of water vapor in
1086 clouds. *J. Atmos. Sci.*, **60**, 2957–2974.

1087 Kumar, B., P. Götzfried, J. Schumacher, and R. A. Shaw, 2018: Scale
1088 dependence of cloud microphysical response to turbulent entrainment
1089 and mixing. *J. Adv. Model Earth Sy.*, **10**, 2777–2785.

1090 Kumar, B., J. Schumacher, and R. A. Shaw, 2013: Cloud microphysical
1091 effects of turbulent mixing and entrainment. *Theor. Comput. Fluid*
1092 *Dyn.*, **27**, 361–376.

1093 Kumar, B., J. Schumacher, and R. A. Shaw, 2014: Lagrangian mixing

dynamics at the cloudy-clear air interface. *J. Atmos. Sci.*, **71**, 2564–2580.

Kunishima, Y., and R. Onishi, 2018: Direct Lagrangian tracking simulation of droplet growth in vertically developing cloud. *Atmos. Chem. Phys.*, **18**, 16619–16630.

Lanotte, A. S., A. Seminara, and F. Toschi, 2009: Cloud droplet growth by condensation in homogeneous isotropic turbulence. *J. Atmos. Sci.*, **66**, 1685–1697.

Lasher-Trapp, S. G., W. A. Copper, and A. M. Blyth, 2005: Broadening of droplet size distributions from entrainment and mixing in a cumulus cloud. *Q. J. R. Meteorol. Soc.*, **131**, 195–220.

Lau, K. M., and H. T. Wu, 2003: Warm rain processes over tropical oceans and climate implications. *J. Geophys. Res.*, **30**, 2290.

Martin, G., D. Johnson, and A. Spice, 1994: The measurement and parameterization of effective radius of droplets in warm stratocumulus clouds. *J. Atmos. Sci.*, **51**, 1823–1842.

McGraw, R., and Y. Liu, 2006: Brownian drift-diffusion model for evolution of droplet size distributions in turbulent clouds. *Geophys. Res. Lett.*, **33**, L03802.

Niedermeier, D., K. Chang, W. Cantrell, K. K. Chandrakar, D. Ciochetto, and R. A. Shaw, 2018: Observation of a link between energy dissipation rate and oscillation frequency of the large-scale circulation in dry and moist rayleigh-benard turbulence. *Phys. Rev. Fluids*, **3**, 083501.

Onishi, R., K. Matsuda, and K. Takahashi, 2015: Lagrangian tracking simulation of droplet growth in turbulence – Turbulence enhancement of autoconversion rate. *J. Atmos. Sci.*, **72**, 2591–2607.

Onishi, R., and A. Seifert, 2016: Reynolds-number dependence of turbulence enhancement on collision growth. *Atmos. Chem. Phys.*, **16**, 12441–12455.

Pope, S. B., 2000: *Turbulent flows*. Cambridge University Press, Cambridge, UK.

Pruppacher, H. R., and J. D. Klett, 1997: *Microphysics of clouds and precipitation 2nd edn.* Springer, 954 pp.

Risius, S., H. Xu, F. D. Lorenzo, H. Xi, H. Siebert, R. A. Shaw, and E. Bodenschatz, 2015: Schneefernerhaus as a mountain research station for clouds and turbulence. *Atmos. Meas. Tech.*, **8**, 3209–3218.

1131 Saito, I., and T. Gotoh, 2018: Turbulence and cloud droplets in cumulus
1132 clouds. *New J. Phys.*, **20**, 023001.

1133 Saito, I., T. Gotoh, and T. Watanabe, 2018: Size distribution spectrum of
1134 noninertial particles in turbulence. *Phys. Rev. E*, **97**, 053108.

1135 Sardina, G., F. Picano, L. Brandt, and R. Caballero, 2015: Continuous
1136 growth of droplet size variance due to condensation in turbulent
1137 clouds. *Phys. Rev. Lett.*, **115**, 1–5.

1138 Sardina, G., F. Picano, L. Brandt, and R. Caballero, 2018: Broadening of
1139 cloud droplet size spectra by stochastic condensation: effects of mean
1140 updraft velocity and ccn activation. *J. Atmos. Sci.*, **75**, 451–467.

1141 Sato, Y., S.-I. Shima, and H. Tomita, 2018: Numerical convergence of shal-
1142 low convection cloud field simulations: Comparison between double-
1143 moment Eulerian and particle-based Lagrangian microphysics cou-
1144 pled to the same dynamical core. *J. Adv. Model. Earth Syst.*, **10**,
1145 1495–1512.

1146 Sedunov, Y. S., 1974: *Physics of Drop Formation in the Atmosphere*. John
1147 Wiley and Sons, 234 pp.

1148 Seifert, A., L. Nuijens, and B. Stevens, 2010: Turbulence effects on warm-

rain autoconversion in precipitating shallow convection. *Q. J. R. Meteorol. Soc.*, **136**, 1753–1762.

Shaw, R. A., 2003: Particle-turbulence interactions in atmospheric clouds. *Annu. Rev. Fluid Mech.*, **35**, 183–227.

Shima, S.-I., K. Kusano, A. Kawano, T. Sugiyama, and S. Kawahara, 2009: The super-droplet method for the numerical simulation of clouds and precipitation: a particle-based and probabilistic microphysics model coupled with a non-hydrostatic model. *Q. J. R. Meteorol. Soc.*, **135**, 1307–1320.

Siebert, H., K. Lehmann, and M. Wendisch, 2006: Observations of small-scale turbulence and energy dissipation rates in the cloudy boundary layer. *J. Atmos. Sci.*, **63**, 1451–1466.

Siebert, H., and R. A. Shaw, 2017: Supersaturation fluctuations during the early stage of cumulus formation. *J. Atmos. Sci.*

Siebert, H., R. A. Shaw, J. Ditas, T. Schmeissner, S. P. Malinowski, E. Bodenschatz, and H. Xu, 2015: High-resolution measurement of cloud microphysics and turbulence at a mountaintop station. *Atmos. Meas. Tech.*, **8**, 3219–3228.

1167 Siewert, R., J. Bec, and G. Krstulvic, 2017: Statistical steady state in
1168 turbulent droplet condensation. *J. Fluid Mech.*, **810**, 254–280.

1169 Sundaram, S., and L. R. Collins, 1997: Collision statistics in an isotropic
1170 particle-laden turbulent suspension. Part 1. Direct numerical simu-
1171 lations. *J. Fluid Mech.*, **335**, 75–109.

1172 Tennekes, H. T., and J. L. Lumley, 1972: *A first course in turbulence*. The
1173 MIT Press.

1174 Vaillancourt, P. A., and M. K. Yau, 2000: Review of particle-turbulence
1175 interactions and consequences for cloud physics. *Bull. Amer. Meteor.*
1176 *Soc.*, **81**, 285–298.

1177 Vaillancourt, P. A., M. K. Yau, P. Bartello, and W. W. Grabowski, 2002:
1178 Microscopic approach to cloud droplet growth by condensation. Part
1179 ii: Turbulence, clustering, and condensational growth. *J. Atmos.*
1180 *Sci.*, **59**, 3421–3435.

1181 Vaillancourt, P. A., M. K. Yau, and W. W. Grabowski, 2001: Microscopic
1182 approach to cloud droplet growth by condensation. Part 1: Model
1183 description and results without turbulence. *J. Atmos. Sci.*, **58**, 1945–
1184 1964.

1185 Wyngaard, J. C., 2010: *Turbulence in the Atmosphere*. Cambridge Univer-
1186 sity Press, 393.

List of Figures

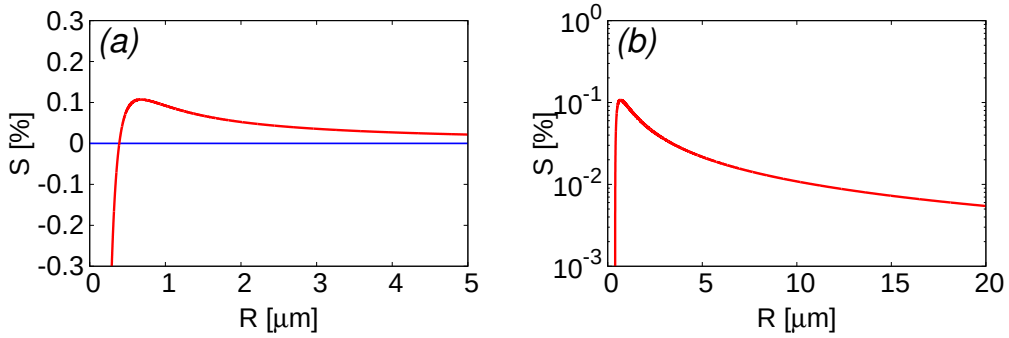

Fig. 1. (a) The Köhler curve $f(R) = (A/R) - (B/R^3)$, where R is the droplet radius of μm, $A = 1.089 \times 10^{-7}$ cm^{-1} and $B = 1.665 \times 10^{-16}$ cm^{-3}. The horizontal line indicates zero. (b) Same as (a) except that the vertical axis is on a logarithmic scale and the range of R is extended to 20 μm.

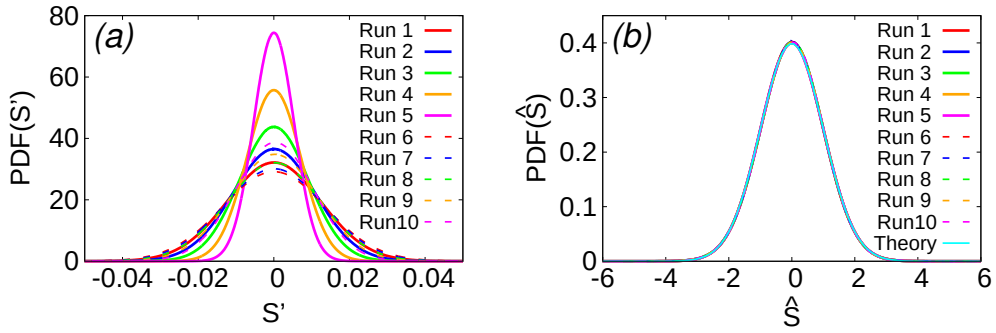

Fig. 2. (a) PDFs for the supersaturation fluctuation in the statistically steady state for Run1–Run10. (b) Same as (a) but the results of each experiment are normalized by the variance. The cyan curve indicates the Gaussian distribution with a zero mean and unit variance: $(2\pi)^{-1/2}\exp(-\hat{S}^2/2)$.

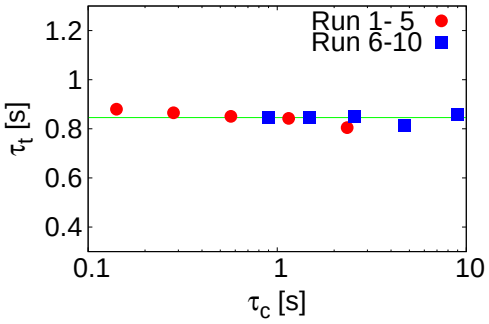

Fig. 3. Estimates of τ_t obtained by substituting the result of each experiment into the right side of (41). The horizontal axis is the phase relaxation time τ_c for each experiment. The horizontal line indicates the average 0.85 (See the text for details).

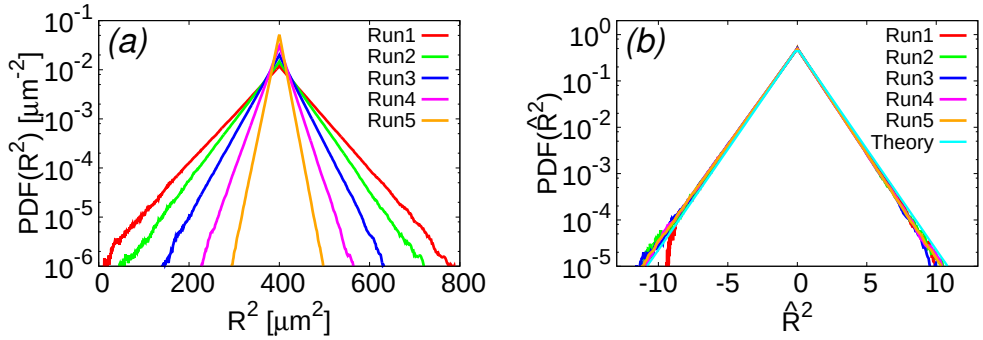

Fig. 4. (a) PDFs of the squared radius (R^2) in statistically steady states for Run1–Run5. (b) Same as (a) but the results of each experiment are normalized by (42). The cyan curve indicates the theoretical curve: $\frac{1}{2}\exp(-|\hat{R}^2|)$ (See the text for details).

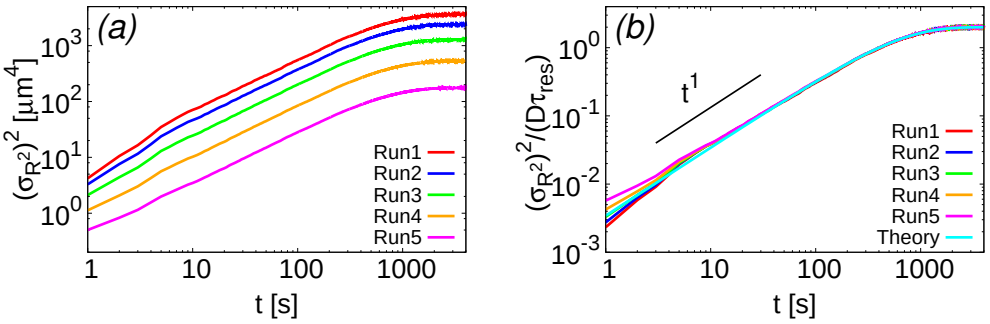

Fig. 5. (a) Time evolution of the variance of the squared radius ($\sigma^2_{R^2}$) for Run1–Run5. (b) Same as (a) but the results of each experiment are normalized by $D\tau_{\rm res}$ (See the text for details). The cyan curve indicates the theoretical curve: $2(1-{\rm e}^{-t/\tau_{\rm res}})$. The short line indicates a slope of 1.

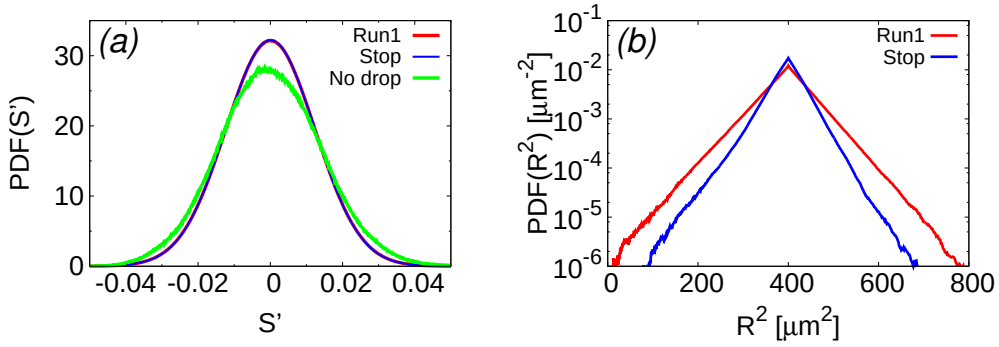

Fig. 6. Comparison of the results between Run1 and the additional experiment which is the same as Run1 except that the particles are stopped (indicated by "stop"). (a) PDFs for the supersaturation fluctuation in statistically steady states. (b) PDFs for the squared radius (R^2) of cloud droplets in statistically steady states. "No drop" in the left panel indicates results for simulations without particles.

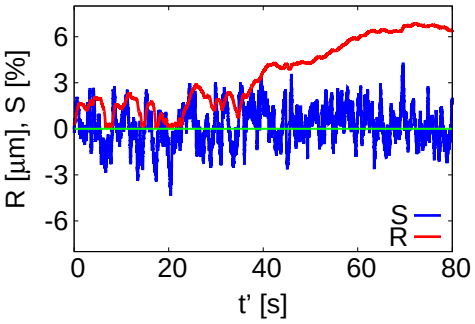

Fig. 7. Time evolution of the droplet radius (R, red curve) and supersaturation at the droplet position (S, blue curve) for a single particle in Run6. The horizontal line indicates zero. Note that the time t' for the horizontal axis starts from the moment after the system has attained a statistically steady state (4000 s after the beginning of the simulation).

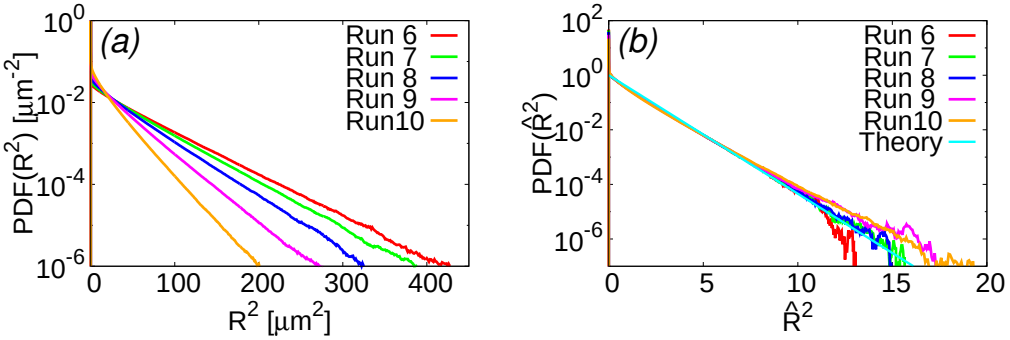

Fig. 8. (a) PDFs of the squared radius (R^2) in statistically steady states for Run6–Run10. (b) Same as (a) but the results of each experiment are normalized by (46). The cyan curve indicates the theoretical curve: $\exp(-\hat{R}^2)$ (See the text for details).

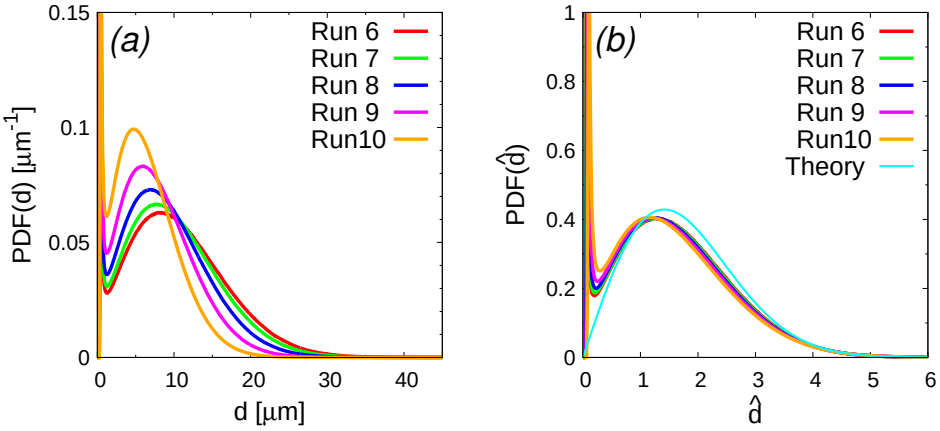

Fig. 9. (a) PDFs for the diameter (d) of cloud droplets in statistically steady states for Run6–Run10. (b) Same as (a) but the results of each experiment are normalized by (50). The cyan curve indicates the theoretical curve: $(\hat{d}/2)\exp(-\hat{d}^2/4)$ (See the text for details).

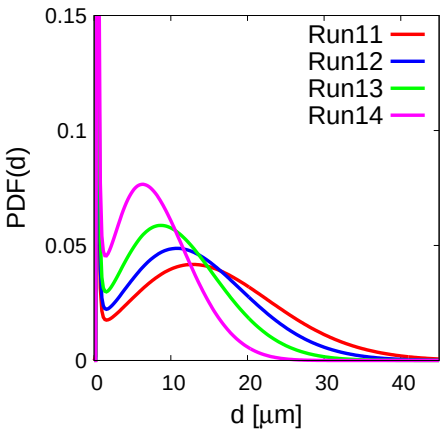

Fig. 10. PDFs for the diameter (d) of the cloud droplets in statistically steady states for Run11–Run14.

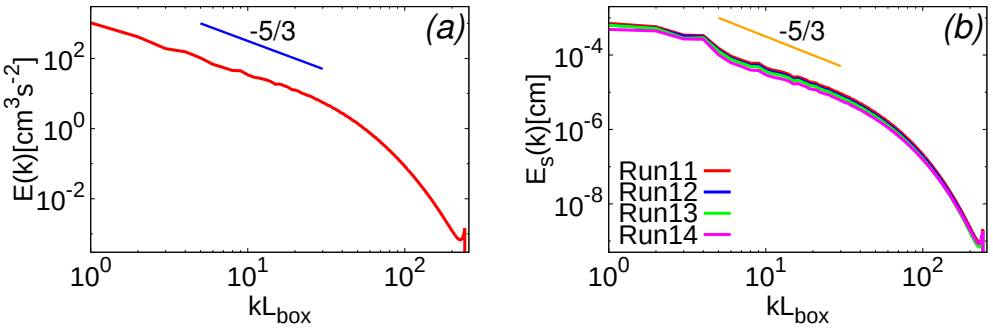

Fig. 11. (a) Time-averaged kinetic energy spectrum for Run11. Other runs (Run12–Run14) have similar kinetic energy spectra. (b) Time-averaged variance spectra of the supersaturation for Run11–Run14. The short line in each panel indicates a slope of -5/3.

List of Tables

Density of liquid water	ρ_{w}	1.0	[g cm^{-3}]
Density of air	ρ_{a}	1.217×10^{-3}	[g cm^{-3}]
Kinematic viscosity of dry air	ν_{a}	1.480×10^{-1}	[cm^{2}s^{-1}]
Thermal diffusivity	κ_T	2.09×10^{-1}	[cm^{2}s^{-1}]
Diffusivity of water vapor	κ_{v}	2.49×10^{-1}	[cm^{2}s^{-1}]
Environmental pressure	P_0	1013.25	[hPa]
Latent heat of vaporization	L_{v}	2.5×10^{10}	[cm^{2}s^{-2}]
Gas constant for dry air	R_{d}	287×10^4	[cm^{2}s^{-2}K^{-1}]
Gas constant for water vapor	R_{v}	462×10^4	[cm^{2}s^{-2}K^{-1}]
Specific heat at constant pressure	c_{p}	1005×10^4	[cm^{2}s^{-2}K^{-1}]
Diffusion coefficient in (31)	K_{s}	1.097×10^{-6}	[cm^{2}s^{-1}]
Temperature for nudging	T_0	290	[K]
Vapor mixing ratio for nudging	Q_0	1.18×10^{-2}	

Table 1. Definitions of parameters and their corresponding values in the present DNS.

R_λ	$u_{\rm rms}$ [cm s^{-1}]	ϵ [cm^{2}s^{-3}]	$\mathcal{L}$ [cm]	λ [cm]	$\eta_{\rm K}$ [cm]	$k_{\rm max}\eta_{\rm K}$	$T_{\rm E}$ [s]	$\tau_{\rm K}$ [s]
52.1	5.38	31.8	3.08	1.43	0.101	2.93	0.576	0.0692
207	9.60	20.4	21.0	3.20	0.113	1.58	2.19	0.0865

Table 2. Mean turbulence parameters. R_λ is the Taylor microscale Reynolds number, $u_{\rm rms}$ is the root-mean-square velocity, ϵ is the mean energy dissipation rate per unit mass, $\mathcal{L}$ is the integral scale, λ is the Taylor microscale, $\eta_{\rm K}$ is the Kolmogorov length, $k_{\rm max}\eta$ is the cut off wavenumber normalized by the Kolmogorov length, $T_{\rm E}$ is the large-eddy turnover time, and $\tau_{\rm K}$ is the Kolmogorov time. Top: small-scale DNS. Bottom: large-scale DNS.

Run	Köhler	R_0 [μm]	$\overline{R}$ [μm]	J_0 [10^{-1} cm^{-3}s^{-1}]	$\overline{n_{\rm d}}$ [cm^{-3}]	$\tau_{\rm c}$ [s]
1	No	20	20	1.3	77	2.3
2	No	20	20	2.7	160	1.1
3	No	20	20	5.5	320	0.57
4	No	20	20	11	640	0.28
5	No	20	20	22	1280	0.14
6	Yes	0.39	5.2	1.3	77	9.0
7	Yes	0.39	4.9	2.7	160	4.7
8	Yes	0.39	4.4	5.5	320	2.6
9	Yes	0.39	3.8	11	640	1.5
10	Yes	0.39	3.1	22	1280	0.90
11	Yes	0.39	7.5	0.34	20	24.1
12	Yes	0.39	6.3	1.3	80	7.2
13	Yes	0.39	5.1	3.4	200	3.6
14	Yes	0.39	3.8	8.6	500	1.9

Table 3. Experimental setups for cloud droplets and their statistics at steady states for the small-scale DNS (Run1–Run10) and the large-scale DNS (Run11–Run14). R_0 is the initial radius of cloud droplets, $\overline{R}$ is the mean droplet radius in the statistically steady state, J_0 is the injection rate of cloud droplets, $\overline{n_{\rm d}}$ is the mean number density of cloud droplets in the statistically steady state, and $\tau_{\rm c}$ is the phase relaxation time estimated from (57). "Yes"/"No" in the second column "Köhler" indicates that the growth equation (31) is integrated with/without terms including A and B, respectively.

Run	σ_S [%]	$\sigma_{S_0}(\tau_\mathrm{s}/\tau_\mathrm{t})^{1/2}$ [%]	τ_s [s]	τ_c [s]
1	1.2	1.2	0.62	2.3
2	1.1	1.1	0.49	1.1
3	0.91	0.92	0.34	0.57
4	0.72	0.72	0.21	0.28
5	0.54	0.55	0.12	0.14
6	1.4	1.4	0.77	9.0
7	1.3	1.3	0.72	4.7
8	1.3	1.3	0.64	2.6
9	1.2	1.2	0.54	1.5
10	1.0	1.0	0.44	0.90

Table 4. Statistics for the supersaturation fluctuation for the small-scale DNS. σ_S is the standard deviation for the supersaturation, $\sigma_{S_0}(\tau_\mathrm{s}/\tau_\mathrm{t})^{1/2}$ is the theoretical value from (5), τ_s is the system timescale (7), τ_c is the phase relaxation timescale, and $\tau_t = 0.85$ s is used (See the text for details).

Run	σ_{R^2} [μm^2]	T0 [μm^2]	τ_{cor} [s]	τ_{s} [s]	τ_{c} [s]
1	60	59	0.41	0.62	2.3
2	49	49	0.36	0.49	1.1
3	36	36	0.28	0.34	0.57
4	23	24	0.19	0.21	0.28
5	13	14	0.12	0.12	0.14

Table 5. Statistics for the droplet size distributions in steady states for Run 1–5. σ_{R^2} is the standard deviation of the squared radius R^2, "T0" is the theoretical value for σ_{R^2} from (18), τ_{cor} is the Lagrangian autocorrelation time of the supersaturation fluctuation, τ_{s} is the system timescale, and τ_{c} is the phase relaxation timescale. $\tau_t = 0.85$ s is used for τ_{s}.

Run	σ_{R^2} [μm^2]	T0 [μm^2]	T1 [μm^2]	T2 [μm^2]	$\overline{S}$ [10^{-2} %]	τ_{cor} [s]	τ_{s} [s]	τ_{c} [s]
6	41	51	49	43	-0.37	0.50	0.77	9.0
7	37	47	43	38	-0.64	0.45	0.72	4.7
8	31	43	37	32	-0.97	0.42	0.64	2.6
9	24	38	30	26	-1.3	0.38	0.54	1.5
10	17	32	23	19	-1.5	0.33	0.44	0.90

Table 6. Statistics for the droplet size distributions in steady states for Run 6–10. σ_{R^2} is the standard deviation of the squared radius R^2, "T0" is the theoretical value for σ_{R^2} from (22), "T1" is the theoretical value from (56) with the mean supersaturation $\overline{S}$ in the 6th column, "T2" is the same as T1 except that $\overline{S}$ is replaced by $\overline{S} - S_{\mathrm{K}}$ where $S_{\mathrm{K}} = 10^{-2}\%$, $\overline{S}$ is the mean supersaturation, τ_{cor} is the Lagrangian autocorrelation time for the supersaturation fluctuation, τ_{s} is the system timescale, and τ_{c} is the phase relaxation timescale. $\tau_t = 0.85$ s is used for τ_{s}. See the text for details of T1 and T2.

Run	σ_S [%]	$\sigma_{S_0}(\tau_\mathrm{s}/\tau_\mathrm{t})^{1/2}$ [%]	τ_s [s]	τ_c [s]
11	1.3	1.3	3.3	24.1
12	1.1	1.1	2.5	7.2
13	0.97	0.97	1.8	3.6
14	0.79	0.81	1.3	1.9

Table 7. Same as Table 4 but for the large-scale DNS (Run11–Run14). $\tau_t = 3.82$ s is used (See the text for details).

Run	σ_{R^2} [μm^2]	T0 [μm^2]	T1 [μm^2]	T2 [μm^2]	$\overline{S}$ [10^{-2} %]	τ_{cor} [s]	τ_{s} [s]	τ_{c} [s]
11	87	125	93	83	-0.63	1.83	3.3	24.1
12	63	94	74	59	-1.54	1.53	2.5	7.2
13	42	70	59	42	-2.14	1.31	1.8	3.6
14	25	48	43	26	-2.48	1.02	1.3	1.9

Table 8. Same as Table 6 but for the large-scale DNS.

Molecular weight for water	$M_{\rm w}$	18.02	[g mol^{-1}]
Surface tension of water	$\sigma_{\rm w}$	72.75×10^{-7}	[J cm^{-2}]
Gas constant for ideal gas	$R_{\rm g}$	8.3	[J K^{-1} mol^{-1}]
Ambient temperature	T_A	290	[K]
Mass of solute	$m_{\rm s}$	1.13×10^{-15}	[g]
Molecular weight for solute	$M_{\rm s}$	58.44	[g mol^{-1}]
Molal osmotic coefficient	Φ_s	1	
Total number of ions a salt molecule dissociates into	$\nu_{\rm s}$	2	

Table 9. Parameters for the Köhler curve. The solute is NaCl (sodium chloride). $m_{\rm s} = 1.13 \times 10^{-15}$g of NaCl corresponds to a sphere with a 50 nm radius and a density $\rho_{\rm s} = 2.16$ g cm^{-3}.